University of California
Santa Barbara

On the Stochastic Closure Theory of Homogeneous Turbulence

A dissertation submitted in partial satisfaction
of the requirements for the degree

Doctor of Philosophy
in
Mathematics

by

John Max Kaminsky

Committee in charge:

Professor Björn Birnir, Chair
Professor Jean-Pierre Fouque
Professor Eckart Meiburg

September 2017

The Dissertation of John Max Kaminsky is approved.

Professor Jean-Pierre Fouque

Professor Eckart Meiburg

Professor Björn Birnir, Committee Chair

June 2017

On the Stochastic Closure Theory of Homogeneous Turbulence

by

John Max Kaminsky

For Austin

Acknowledgements

The author would like to acknowledge the contributions of several people to this dissertation. First, the author would like to acknowledge Gregory P. Bewley, Michael Sinhuber, and the Max Planck Institute for Self-Organization and Dynamics for contributing the wind tunnel data used in Chapter 3 of this dissertation to analyze homogeneous turbulence. The author would also like to acknowledge Joe Klewicki and the University of New Hampshire, who provided the wall data used in Chapter 4 to analyze the Townsend-Perry constants. The author would also like to acknowledge the invaluable contributions of his advisor, Professor Björn Birnir, and the members of his committee, Professors Jean-Pierre Fouque and Eckart Meiburg.

Finally, the author would like to acknowledge the graduate staff advisor Medina Price, as well as his family and friends, without whom this dissertation would not be possible.

Curriculum Vitæ

John Max Kaminsky

Education

2017	Ph.D. in Mathematics (Expected), University of California, Santa Barbara.
2014	M.A. in Physics, University of California, Santa Barbara.
2010	B.A. in History and Math, State University of New York, Cortland

Publications

1. *Reynolds Number Dependence of the Structure Functions in Homogeneous Turbulence.* (With Björn Birnir, Gregory P. Bewley, and Michael Sinhuber). Submitted.

2. *Reynolds Number Dependence of the Townsend-Perry Constants.* (With Björn Birnir and Joe Klewicki). In preparation.

Abstract

On the Stochastic Closure Theory of Homogeneous Turbulence

by

John Max Kaminsky

We compare the predictions of the stochastic closure theory (SCT) [1] with experimental data obtained in the Variable Density Turbulence Tunnel (VDTT) [2], at the Max Planck Institute for Dynamics and Self-Organization in Göttingen. The mean flow in the homogeneous turbulence experiment reduces the number of parameters in SCT to just three, one characterizing the variance of the mean field noise and another characterizing the rate in the large deviations of the mean. The third parameter is the decay exponent of the Fourier variables in the Fourier expansion of the noise. This characterizes the smoothness of the turbulent velocity.

We compare the data for the even-order longitudinal structure functions ranging from the the second to the eighth structure function as well as the third-order structure function, to the SCT theory with generic noise, depending on the above three parameters, at five Taylor-Reynolds (R_λ) numbers ranging from 110 to 1450. The theory gives excellent comparisons with data for all the structure functions and for all the Taylor-Reynolds numbers. This highlights the advantage of the SCT theory, where the structure functions can be computed explicitly and their dependence on the R_λ number computed. These results are robust with respect to the size of dissipation range filters applied to the data, and comparisons to the fits without the R_λ number corrections show a clear improvement when the corrections are present. This improvement is significant for the lower R_λ number and disappears as the R_λ number becomes large, as expected.

Very surprisingly the comparison of SCT and the data also gives information about the smoothness of the turbulent velocity as R_λ becomes very large.

We then compare the SCT to the Townsend-Perry constants generated in the flow physics facility (FPF) at the University of New Hampshire. The Reynolds correction terms in the SCT changed the initial derivation of this similarity, forcing a refinement of the theory. Once done, we see good agreement between the data and the SCT.

Contents

Chapter 1

Introduction

The mathematical theory of turbulence has its roots in the work of Kolmogorov. In 1941, Kolmogorov published his celebrated four-fifths law and postulated, with Obukhov, that the structure functions of turbulence should scale with lag variable, i.e.

$$S_p(x,y,t) = E(|u(x,t) - u(y,t)|^p) = C_p r^{\frac{p}{3}},$$

where p is the order of the structure function and $r = |x-y|$. Lev Landau would immediately criticize this theory for not taking into account the influence of the large scale flow structure and the influence of intermittency, the development of long tails in the velocity difference distributions at large Reynolds numbers, see [3]. In 1962, Kolmogorov and Obukhov revised their theory to address these criticisms. They introduced a correction term to the exponent, i.e.

$$S_p(x,y,t) = C_p < \varepsilon^{\frac{p}{3}} > r^{\frac{p}{3}} = C'_p r^{\frac{p}{3}+\tau_p} = C'_p r^{\zeta_p},$$

where ε is the dissipation rate and $\zeta_p = \frac{p}{3} + \tau_p$. The form of this correction was modeled by She and Leveque in 1994 to be

$$\tau_p = -\frac{2p}{9} + 2(1 - (\frac{2}{3})^{\frac{p}{3}}), \tag{1.1}$$

see [4], and derived from the Navier-Stokes equations by Birnir in [1] . In [1], the log-Possonian processes of Dubrulle [5] and She and Waymire [6], responsible for the intermittency corrections, were derived from the stochastic Navier-Stokes equation.

Kolmogorov and Obukhov considered the velocity in turbulent flow to be a stochastic process and their hypothesis can be interpreted to say, see [7], that the N-point velocity probability distribution function (PDF) of turbulence does not depend on x or y individually but only on r and ν and ε. Moreover, when $r >> \eta$, where η is the Kolmogorov (dissipation) scale, then the PDF only depends on ε and r and is independent of the viscosity ν. Since the 2-point PDF determines the structure functions the same statements apply to them.

If the turbulent velocity is a stochastic process it must satisfy a stochastic Navier-Stokes equation and such an equation was formulated by Landau and Lifschitz in their Fluid Dynamics book [3] in 1959. They considered the noise in the stochastic Navier-Stokes equation to be the fluctuations in the fluid, that cannot be ignored in fully developed turbulence, and argued that it should be white both in time and space. The latter assumption cannot be true, the Navier-Stokes equation driven by noise that is white in space produces velocities the are not continuous in three dimensions, see [8], and this is not observed in nature. Birnir [1] argued that the noise has enough smoothness in space that the dissipation rate ε was finite and of a generic nature, including an additive term corresponding to a mean-field noise and another corresponding to the large deviations of the mean-field. He also added a multiplicative noise term, modeling jumps in the gradient for the flow velocity, and was able to show that this term produced the log-Poisson processes of Dubrulle, She and Waymire and their intermittency corrections τ_p. These assumptions are the basis of the Stochastic Closure Theory (SCT) [9].

In Chapter 2, we shall give an overview of the SCT. We start by laying out the basic assumptions of the SCT. We start with the Navier-Stokes equation, to which we apply the classical Reynolds Decomposition. To find a closure rule for the Reynolds stress term, we write down a stochastic partial differential equation with additive and multiplicative noise added to

the Navier-Stokes equations. We describe the derivation of these noise terms from the physical properties of the flow. Once we have written down the model, we describe how to explicitly solve for the structure functions. Finally, we describe how we can pass from the three-dimensional Navier-Stokes equation, and its related structure functions, to the one-dimensional stream-wise velocity structure functions.

In Chapter 3. we describe the results of fitting the mathematical model to data generated by the Variable Density Turbulence Tunnel in Göttingen, Germany. We start with an overview of wind tunnel experiments and the fitting routine. We ultimately see excellent agreement between the mathematical model and the data. We then give an overview of various tests performed to ensure the accuracy of the model. Namely, we demonstrate the importance of the Reynolds Number corrections in the formulas, thereby showing how the flow is affected by the Reynolds Number. We also ensure that the fitting routines are robust to the experimental conditions. We ultimately get suprising results from the fits, showing how the smoothness of the flow is potentially impacted by the Reynolds Number.

In Chapter 4, we describe the application of the SCT to the Townsend-Perry constants. To do this, we utilize data generated in the flow physics facility (FPF) at the University of New Hampshire. First, we give an overview of the Townsend-Perry constants. We then give an alternative formulation of the constants, using a similarity hypothesis instead of the standard Attached Eddy hypothesis. We then attempt to use the theory developed by Birnir and Chen in [10] to show a relationship between the Townsend-Perry and constants and the SCT. This proved ineffective, due to the fact that Birnir and Chen compensated by C_1 instead of $C_2^{\frac{1}{2}}$. We then amended the theory and show that $C_2^{\frac{1}{2}}$ is the correct compensation term.

Two appendices are also included. Appendix A contains all the figures for this dissertation and will be referenced throughout. Appendix B contains a sample of the Mathematica code used in Chapter 3.

1.1 Permissions and Attributions

1. The content of chapters 1, 2, 3 and both appendices is the result of a collaboration with Gregory P. Bewley and Michael Sinhuber, and is currently submitted. The content of chapters 1 and 4, as well as appendix A, is the result of a collaboration with Joe Klewicki.

Chapter 2

The Stochastic Closure Theory

2.1 The Assumptions of SCT and Its Predictions

The Stochastic Closure Theory (SCT) is based on the following assumptions:

SCT Assumptions:

1. The small scale flow in fully developed turbulence satisfies a stochastic Navier-Stokes (SNS) equation.

2. The noise in the SNS consists of both an additive and a multiplicative term.

3. The additive noise term is a general mean field noise that has enough spatial smoothness for the dissipation rate
$$\varepsilon = \nu \int_\Omega |\nabla u|^2 dx < \infty,$$
to be finite. In addition to this "infinite-dimensional Brownian" mean-field noise, there is a deterministic additive term that estimates the large-deviations of the mean-field.

4. The multiplicative noise term consists of pure jumps, modeling jumps in the velocity gradient ∇u, multiplied by the velocity u.

5. The most singular (having least spatial smoothness) structures in (3-d) turbulence are one-dimensional vortex lines.

These assumptions produce the Stochastic Navier-Stokes equation (2.6) below. The detailed arguments leading to the form of the noise are given in [1] and [9]. They follow the spirit of the argument in Landau and Lifschitz [3].

The predictions of the SCT theory is the Kolmogorov-Obukhov '62 theory of turbulence, with the She-Leveque intermittency corrections, in all quantitative detail. In particular,

SCT Predictions:

1. The structure functions of turbulence are given by explicit formulas.

2. The Reynolds number dependence of the structure functions is also given explicitly.

3. The N-point probability density functions of turbulence exists and can be computed. In the 2-point case, it is determined by the Kolmogorov-Hopf functional differential equation, see [9], and has an explicitly formula, see [11].

4. The PDF for the velocity distribution in turbulence is a Generalized-Hyperbolic distribution [12] convolved with the Poisson distribution of the log-Poisson processes of Dubrulle, She and Waymire, see [11].

The most important SCT prediction for this dissertation is number 2, that we have an explicit formula for the structure functions with their Reynolds number dependence given. This means that we can use these formulas to fit the data measured in the VDTT and this is the subject of chapter 3. The disadvantage when we consider equation (2.6) is that the noise has infinitely many undetermined coefficients c_k, d_k and h_k. The last coefficients are fixed by the assumption number 4 above. Namely, that the vorticity lines are one-dimensional implies that all the coefficients h_k are fixed, see [9]. But we are still left with infinitely many coefficients

c_k, d_k. The miraculous fact is that the comparison with the VDTT data reduces these coefficients to only three. When the mean flow is given, we get one parameter characterizing the infinite-dimensional Brownian, another parameter characterizing the large deviation of the mean and one power characterizing both, or their spatial smoothness. Of course the mean flow and these three parameters depend on the Taylor-Reynolds number but not on the order of the structure functions. The upshot is a much improved stochastic closure model (3.2) with only three parameters characterizing the noise.

2.2 The Stochastic Closure Model and the Structure Functions

In this section, we describe the calculation of the structure functions of turbulence, which will be compared with the experimental data. The flow in the wind tunnel is governed by the Navier Stokes equation:

$$\begin{aligned} u_t + (u \cdot \nabla)u &= \nu \Delta u - \nabla p, \\ \operatorname{div} u &= 0, \\ u(x,0) &= u_0(x), \end{aligned} \tag{2.1}$$

where $u(x)$ is the fluid velocity, $x \in \mathbb{R}^3$, p is pressure, and ν is the viscosity. We also impose periodic boundary conditions upon the flow. The second line in (2.1) is the incompressibility condition. Using the incompressibility, we can eliminate the pressure to get

$$u_t + u \cdot \nabla u = \nu \Delta u + \nabla(\Delta^{-1}[\operatorname{Trace}(\nabla u)]^2). \tag{2.2}$$

This equation defines the evolution (or flow) of the velocity of the fluid in time. We will impose periodic boundary conditions on the small scales below.

Following the classical Reynolds decomposition [13], we decompose the velocity into mean flow U and the fluctuations u. Then the velocity is written as $U+u$, where U describes the mean, or large scale flow and u describes the velocity fluctuations. These two terms describe the large scales and small scales of the flow, respectively. We must also decompose the pressure into mean pressure P and the fluctuations p, then the equation for the large scale flow can be written as

$$U_t + U\cdot\nabla U = \nu\Delta U - \nabla P - \nabla\cdot(\overline{u\otimes u}), \tag{2.3}$$

where in coordinates $\nabla\cdot(\overline{u\otimes u}) = \frac{\partial\overline{u_iu_j}}{\partial x_j}$, that is ∇ is dotted with the rows of $\overline{u_iu_j}$, and $R_{ij} = \overline{u\otimes u}$ is the Reynolds stress, see [14]. The Reynolds stress has the interpretation of a turbulent momentum flux and the last term in (2.3) is also know as the eddy viscosity. It describes how the small scales influence the large scales. In addition we get divergence free conditions for U, and u

$$\nabla\cdot U = 0, \qquad \nabla\cdot u = 0.$$

Together, (2.3) and the divergence free condition on U give the Reynolds Averaged Navier-Stokes (RANS) that forms the basis for most contemporary simulations of turbulent flow. The large scale equation (2.3) is satisfied by the mean flow $U =$ constant in the measurement region of the VDTT. Thus in our case (2.3) reduces to the pressure gradient balancing the eddy viscosity.

Finding a constitutive law for the Reynolds stress $\overline{u\otimes u}$ is the famous closure problem in turbulence and we will solve that by writing down a stochastic equation for the small scale velocity u. This was first done by Landau and Lifschitz in [3].

The consequence of the SCT hypothesis is that the fluctuating velocity u in turbulence is a stochastic process that is determined by a stochastic partial differential equation (SPDE). It will be the Navier-Stokes equation for the fluctuations driven by noise, see below. This is the point of view taken by Kolmogorov in [15, 16, 17], but the question we have to answer is: what

is the form of the noise? There is a large literature on this question, trying to trace the form of the noise back to the fluid instabilities, but these attempts have proven to be unsuccessful. Any memory of the fluid instabilities is quickly forgotten in fully-developed turbulence and the noise seems to be of a general form. Thus it makes sense to try to put generic noise into the Navier-Stokes equations and see how the Navier-Stokes evolution colors generic noise. Below we will answer what generic noise in the Navier-Stokes equation must look like, see [9] for more details.

For fully developed turbulence, we close the model with a stochastic forcing term to account for the small scales in (2.1). This noise term models the dissipation in the flow. We impose periodic boundary conditions and then discretize on the torus. Let p_k denote the dissipation process in the j-th box. We assume these dissipation processes in the flow are weakly coupled and have mean m. Thus, the average is given by

$$M_n = \frac{1}{n}\sum_{j=1}^{n} p_j.$$

We now make use of the Central Limit Theorem:

Theorem 2.2.1 *Suppose that $\{X_k\}$ is an independent sequence of random variables, with the same distribution, with mean m and finite positive variance σ^2. Then,*

$$\lim_{n\to\infty} \frac{\sqrt{n}(M_n - m)}{\sigma} = \mathcal{N}(0,1)$$

in distribution, where

$$M_n = \frac{X_1 + X_2 + \cdots + X_n}{n}.$$

For the proof of the Central Limit Theorem, see page 194 in [18]. Thus, M_n will converge to a Gaussian distribution with mean zero and variance one. Then, define

$$x_t^n = \frac{S_{[tn]} - nm}{\sqrt{n}\sigma},$$

where $S_n = \sum_{j=1}^{n} p_j$ and $[tn]$ denotes integer value. We now apply the Functional Central Limit Theorem, as given by Theorem 8.1 in [19], and so the processes x_t^n must converge in distribution to a Brownian motion b_t as $n \to \infty$. This must occur in the direction of any Fourier component and so we get

$$\bar{D} = \sum_{k \neq 0} c_k^{\frac{1}{2}} db_t^k e_k(x),$$

where $e_k(x) = e^{2\pi i k x}$ are distinct Fourier compoents complete with its own Brownian motion b_t^k, and $c_k^{\frac{1}{2}}$ are coefficients that converge sufficiently fast enough to ensure convergence of the entire series, see [9].

However, there are fluctuations in the mean of the dissipation which can explained via the Large Deviation Principle. To apply the Large Deviation Principle, we need to describe the rate function associated with the process, which depend on whether the fluctuations are random. If they are, the fluctuations can be modeled by a Poisson process with rate λ and furthermore, if there is bias in the fluctuations, then the deviations of M_n are bounded above by a constant determining the direction of the bias times the rate η. Cramer's Theorem, see [9], then gives the rate function is bounded by $\eta = \lambda$, and so the second additive noise terms is

$$D' = \sum_{k \neq 0} d_k \eta_k dt e_k(x).$$

Here, $e_k(x)$ is defined as above, d_k is defined similarly to $c_k^{\frac{1}{2}}$, and η_k are the rates in the k-th direction. We choose $\eta_k = |k|^{\frac{1}{3}}$ to line up with the scaling of the Central Limit Theorem term. Thus, the Large Deviation Principle gives the term

$$D' = \sum_{k \neq 0} d_k |k|^{\frac{1}{3}} dt e_k(x).$$

These two terms defined the additive noise forcing term. A detailed description of these terms is given in [9].

A final forcing term comes from the multiplicative noise. This models jumps in the velocity gradient or vorticity concentrations. If we let N_t^k denote the number of velocity jumps

associated to the k-th wave number that have occured by time t. This in turn implies that the differential

$$dN^k(t) = N^k(t+dt) - N^k(t)$$

denotes the number of jumps in the time interval $(t, t+dt]$. Then the multiplicative noise has the form

$$J = \sum_{k\neq 0} \int_{\mathbb{R}} h_k(t,z)\bar{N}^k(dt,dz),$$

where h_k measures the size of the jump and $\bar{N}^k$ is the compensated number of jumps. For more information on the multiplicative noise, see [9].

Hence, adding the terms $\bar{D}$, D', and J multiplied by u, to the Navier-Stokes equation, we get a stochastic PDE describing the fully developed turbulent small-scale flow in the wind tunnel:

$$\begin{aligned} du + u\cdot\nabla u dt = {} & [\nu\Delta u + \nabla(\Delta^{-1}[\mathrm{Trace}(\nabla u)]) - u\cdot\nabla U - U\cdot\nabla u]dt \\ & + \sum_{k\neq 0} d_k|k|^{\frac{1}{3}} dt e_k(x) + \sum_{k\neq 0} c_k^{\frac{1}{2}} db_t^k e_k(x) \\ & + u\sum_{k\neq 0}\int_{\mathbb{R}} h_k(t,z)\bar{N}^k(dt,dz). \end{aligned} \tag{2.4}$$

We drop the term $-u\cdot\nabla U$, in the equation above, since the mean flow U is approximately constant for homogeneous turbulence, see [2]. We now use Girsanov's Theorem:

Theorem 2.2.2 *Let $y_t \in \mathbb{R}^n$ be an Ito process of the form*

$$dy_t = u(t,\omega)dt + db_t,\ t \leq T,\ y_0 = 0,$$

where $T \leq \infty$ is given and b_t is n-dimensional Brownian motion. Let

$$M_t = e^{(\int_0^t u(s,\omega)db_s - \frac{1}{2}\int_0^t u^2(s,\omega)ds)},$$

where u satisfies Novikov's condition,

$$E(e^{\frac{1}{2}\int_0^T u^2(s,\omega)ds}) < \infty.$$

Define the measure

$$dQ(\omega) = M_T(\omega)d\mathbb{P}(\omega);$$

Then u_t is an n-dimensional Brownian motion with respect to the probability law Q for $t \leq T$.

For the proof of Girsanov's Theorem, see pages $149-151$ of [20]. An application of Girsanov's Theorem allows us to eliminate the $(-u\cdot\nabla u - U\cdot\nabla u)dt$ term at the cost of adding an exponential martingale,

$$M_t = \exp(-\int u(B_s,s)dB_s - \frac{1}{2}\int_0^t |u(B_s,s)|^2 ds),$$

to each term in the Navier Stokes equation:

$$\begin{aligned} du = &[\nu\Delta u + \nabla(\Delta^{-1}[\mathrm{Trace}(\nabla u)])]M_t dt \\ &+ \sum_{k\neq 0} d_k|k|^{\frac{1}{3}} M_t dt e_k(x) + \sum_{k\neq 0} c_k^{\frac{1}{2}} M_t db_t^k e_k(x) \\ &+ u\sum_{k\neq 0}\int_{\mathbb{R}} h_k(t,z)\bar{N}^k M_t(dt,dz). \end{aligned} \tag{2.5}$$

Next, we use the Feynman-Kac Formula:

Theorem 2.2.3 *Let $f \in C_0^2(\mathbb{R}^n)$ and assume that $q \in \mathbb{R}^n$ is bounded from below. Then the function*

$$u(x,t) = E^x(e^{(-\int_0^t q(x_s)ds)} f(x_t))$$

satisfies $u(\cdot,t) \in \mathcal{D}_A$ for each t and u is the unique solution of the initial value problem for the partial differential equation

$$\begin{aligned} \frac{\partial u}{\partial t} &= Au - qu,\ t > 0,\ x \in \mathbb{R}^n, \\ u(x,0) &= f(x),\ \ x \in \mathbb{R}^n. \end{aligned}$$

For the proof of Feynman-Kac Formula, see pages $128-129$ of [20]. The Feynman-Kac Formula allows us to eliminate the term $u\sum_{k\neq 0}\int_{\mathbb{R}} h_k(t,z)\bar{N}^k M_t(dt,dz)$ at the cost of adding a

log-Poisson process

$$e^{\int_s^t dq} = \frac{1}{3}(\sum_{k\neq 0}^{m}\{\int_0^t\int_{\mathbb{R}}\ln(1+h_k)\bar{N}^k(ds,dz)+\int_0^t\int_{\mathbb{R}}(\ln(1+h_k)-h_k)m_k(ds,dz)\})$$

to each term in the Navier-Stokes equation. Thus, the new Navier Stokes equation becomes

$$\begin{aligned} du &= [\nu\Delta u+\nabla(\Delta^{-1}[\text{Trace}(\nabla u)])]e^{\int_s^t dq}M_t dt \\ &+\sum_{k\neq 0} d_k|k|^{\frac{1}{3}}e^{\int_s^t dq}M_t dt e_k(x)+\sum_{k\neq 0}c_k^{\frac{1}{2}}e^{\int_s^t dq}M_t db_t^k e_k(x) \end{aligned} \tag{2.6}$$

$$\tag{2.7}$$

Finally, we use the existence theorem of nonlinear stochastic partial differential equations in infinite-dimensional space:

Theorem 2.2.4 ***Existence Theorem for nonlinear stochastic partial differential equation (SPDE).*** *Consider the initial value SPDE problem*

$$du = (Au+F(t,u))dt+G(t,u)dB_t,,\ u(x,0)=u_0.$$

A stochastic process $u(\omega,x,t)$ is a mild solution of this SPDE IVP if

$$u(t) = e^{At}u_0+\int_0^t e^{A(t-s)}F(s,u(s))ds+\int_0^t e^{A(t-s)}G(s,u(s))dB_s.$$

For the proof, see page 186 in [21]. Now, this theorem does not apply directly here, as the multiplicative noise concerns jumps and not Brownian motion. However, a slight alteration of the proof can give local existence of solutions. Thus, in integral form, the stochastic Navier Stokes equation governing fully developed turbulence is given by

$$\begin{aligned} u &= e^{K(t)}e^{\int_0^t dq}M_t u^0+\sum_{k\neq 0}c_k^{\frac{1}{2}}\int_0^t e^{K(t-s)}e^{\int_s^t dq}M_{t-s}db_s^k e_k(x) \\ &+\sum_{k\neq 0}d_k\int_0^t e^{K(t-s)}e^{\int_s^t dq}M_{t-s}|k|^{\frac{1}{3}}dt e_k(x), \end{aligned} \tag{2.8}$$

where K is the operator

$$K = \nu\Delta + \nabla\Delta^{-1}\text{Trace}(\nabla), \tag{2.9}$$

M_t is the exponential martingale, see below, $e_k(x) = e^{2\pi ikx}$ is a Fourier component complete with its own Brownian motion b_t^k, and the coefficients $c_k^{\frac{1}{2}}$ and d_k decay fast enough so that the series converges, see [9], Chapter 1. Thus, we have that

$$u(x,t) - u(y,t) = \tag{2.10}$$
$$\sum_{k\neq 0}\left[(c_k^{\frac{1}{2}}\int_0^t e^{K(t-s)}e^{\int_s^t dq}M_{t-s}db_s^k + d_k\int_0^t e^{K(t-s)}e^{\int_s^t dq}M_{t-s}|k|^{\frac{1}{3}}ds)(e_k(x)-e_k(y))\right],$$

where $u(x,t)$ and $u(y,t)$ are the flow velocities at two points x and y in the wind tunnel. This permits us to describe the computation of the structure functions:

$$S_p(x-y,t) = E(|u(x,t)-u(y,t)|^p).$$

First, we note that the expectation is actually a composition of two expectations, one for the Brownian motion, denoted E_b and the other for the log-Poisson process, denoted E_p. The log-Poisson expectation acts upon the term

$$e^{\int_s^t dq} = \exp\{\frac{\frac{2}{3}\ln|k| + N_k\ln(\frac{2}{3})}{3}\} = (|k|^{\frac{2}{3}}(\frac{2}{3})^{N_t^k})^{\frac{1}{3}},$$

given by the Feynman-Kac formula, see [9]. Then, we get that

$$E_p([|k|^{\frac{2}{3}}(\frac{2}{3})^{N_t^k}]^{\frac{p}{3}}) = |k|^{-(-\frac{2p}{9}+2(1-(\frac{2}{3})^{\frac{p}{3}}))},$$

see [9]. Notice the exponent above is the She-Leveque intermittency correction (1.1), denoted τ_p. Applying E_p also eliminates all terms $(e_k(x)-e_k(y))(e_j(x)-e_j(y))$ for $k \neq j$. Standard algebra and trigonometry gives

$$e_k(x) - e_k(y) = 2e^{\pi ik(x+y)}\sin(\pi k\cdot(x-y)).$$

Thus, we get that

$$E(|u(x,t)-u(y,t)|^p) = \tag{2.11}$$
$$E(\Big|\sum_{k\neq 0}\Big[(c_k^{\frac{1}{2}}\int_0^t e^{K(t-s)}e^{\int_s^t dq}M_{t-s}db_s^k + d_k\int_0^t e^{K(t-s)}e^{\int_s^t dq}M_{t-s}|k|^{\frac{1}{3}}ds)(e_k(x)-e_k(y))\Big]\Big|^p)$$
$$= E_b(\Big|\sum_{k\neq 0}\Big[(c_k^{\frac{1}{2}}\int_0^t e^{K(t-s)}|k|^{-\tau_p}M_{t-s}db_s^k) + d_k\int_0^t e^{K(t-s)}|k|^{-\tau_p}M_{t-s}|k|^{\frac{1}{3}}ds)\Big]$$
$$\times 2e^{\pi ki(x+y)}\sin(\pi k\cdot(x-y))\Big|^p).$$

Now, we use a eigenvalue estimate for the operator K, replacing it with $\lambda_k = C|k|^{\frac{2}{3}} + 4\nu\pi^2|k|^2$, see [9]. This estimate assumes ergodicity and that the expectation of the norm of u in the Sobolev space $H^{\frac{11}{6}^+}$ is finite, see Lemma 2.7 in [9]. We will discuss this in more detail below. M_t is the exponential martingale:

$$M_t = \mathrm{Exp}[\int (U+u)\cdot dB_s - \int \frac{|U+u|^2}{2}ds],$$

where $B_t \in \mathbb{R}^3$ is an auxiliary Brownian motion and $U+u$ is the Reynolds decomposition of the flow. A simple application of Ito's formula yields

$$M_t^p = 1 + \int_0^t (U+u)M_s\cdot dB_s + \frac{p(p-1)}{2}\int_0^t |U+u|^2 M_s^p ds.$$

Thus, we have

$$\begin{aligned} E[M_t^p] &= 1 + \frac{p(p-1)}{2}\int_0^t E[|U+u|^2 M_s^p]ds \\ &\leq 1 + \frac{p(p-1)}{2}\int_0^t E[|U+u|^4]^{1/2}E[M_s^{2p}]^{1/2}ds \end{aligned}$$

by the Cauchy-Schwarz inequality. A consideration of the fourth-order structure function below shows that last term only contributes higher order (in k) terms to the denominator of the structure functions. We will ignore this small correction term below.

Finally, we take the absolute value and expand the polynomial expression in (2.11). To ultimately compute the structure functions, we use Ito's Lemma

$$E[(\int_S^T f(t,w)dB_t)^2] = \int_S^T E[(f(t,w))^2]dt$$

to turn any even power of the stochastic integral into a deterministic integral, which can then be solved for using standard calculus. For odd powers, we use the fact that

$$E[\int_S^T f dB_t] = 0$$

to eliminate such terms. We then find the first-order structure function is given by

$$\begin{aligned} E(|u(x,t)-u(y,t)|) &= S_1(x,y,t) \\ &= \frac{2}{C}\sum_{k\in\mathbb{Z}^3\setminus\{0\}} \frac{|d_k|(1-e^{-\lambda_k t})}{|k|^{\zeta_1}+\frac{4\pi^2\nu}{C}|k|^{\zeta_1+\frac{4}{3}}}|\sin(\pi k\cdot(x-y))|, \end{aligned} \tag{2.12}$$

where $|\cdot|$ denotes the vector norm in $\mathbb{R}^3$. The second-order structure function is given by

$$\begin{aligned} E(|u(x,t)-u(y,t)|^2) &= S_2(x,y,t) \\ &= \frac{4}{C^2}\sum_{k\in\mathbb{Z}^3}\Big[(|\sin^2(\pi k\cdot(x-y))|) \\ &\Big\{\frac{\frac{C}{2}c_k(1-e^{-2\lambda_k t})}{|k|^{\zeta_2}+\frac{4\pi^2\nu}{C}|k|^{\zeta_2+\frac{4}{3}}} \\ &+\frac{|d_k|^2(1-e^{-\lambda_k t})}{|k|^{\zeta_2}+\frac{8\pi^2\nu}{C}|k|^{\zeta_2+\frac{4}{3}}+\frac{16\pi^4\nu^2}{C^2}|k|^{\zeta_2+\frac{8}{3}}}\Big\}\Big] \end{aligned} \tag{2.13}$$

where $c_k = |c_k^{\frac{1}{2}}|^2$. The third-order structure function is given by

$$\begin{aligned} E(|u(x,t)-u(y,t)|^3) &= S_3(x,y,t) \\ &= \frac{8}{C^3}\sum_{k\in\mathbb{Z}^3}\Big[(|\sin^3(\pi k\cdot(x-y))|) \\ &\Big\{\frac{\frac{C}{2}c_k|d_k|(1-e^{-2\lambda_k t})(1-e^{-\lambda_k t})}{|k|^{\zeta_3}+\frac{8\pi^2\nu}{C}|k|^{\zeta_3+\frac{4}{3}}+\frac{16\pi^4\nu^2}{C^2}|k|^{\zeta_3+\frac{8}{3}}} \\ &+\frac{|d_k|^3(1-e^{-\lambda_k t})^3}{|k|^{\zeta_3}+\frac{12\pi^2\nu}{C}|k|^{\zeta_3+\frac{4}{3}}+\frac{48\pi^4\nu^2}{C^2}|k|^{\zeta_3+\frac{8}{3}}+\frac{64\pi^6\nu^3}{C^3}|k|^{\zeta_3+4}}\Big\}\Big] \end{aligned} \tag{2.14}$$

The general p-th order structure function is given by

$$S_p(x,y,t) = \frac{2^p}{C^p}\sum_{k\neq 0} A_p \times |\sin^p[\pi k\cdot(x-y)]|, \tag{2.15}$$

where

$$A_p = \frac{2^{\frac{p}{2}}\Gamma(\frac{p+1}{2})\sigma_k^p {}_1F_1(-\frac{1}{2}p, \frac{1}{2}, -\frac{1}{2}(\frac{M_k}{\sigma_k})^2)}{|k|^{\zeta_p} + \frac{p_k\pi^2\nu}{C}|k|^{\zeta_p+\frac{4}{3}} + O(\nu^2)}, \tag{2.16}$$

where Γ is the gamma function, ${}_1F_1$ is the hypergeometric function, $M_k = |d_k|(1-e^{-\lambda_k t})$, $\sigma_k = \sqrt{(\frac{C}{2}c_k(1-e^{-2\lambda_k t}))}$, and p_k is different for each denominator term in the series. Note that the Reynolds number dependence is captured via the viscosity term ν. C is a constant approximating the mean velocity of the flow. It will allowed to vary across structure functions to accommodate a relative change in the mean and the large deviations.

2.3 The One-dimensional Structure Functions

We want to fit the structure functions (2.15) to the experimental data collected in the VDTT, but to do this we have to reduces the three-dimensional structure functions to one-dimensional ones. One can consider structure functions where the measurements are take at two distinct points along the length of the tunnel, in the direction of the mean velocity. These are called the longitudinal structure functions, $S_p(r,t)$, where $r = x-y$, is a vector along the main axis of the tunnel. Or, one can consider the transversal structure functions, $S_p(q,t)$, where $q = x-y$, is a vector in the radial direction of the tunnel, perpendicular to r. In homogeneous turbulence these two structure functions are not independent. In fact, one can show, see [7], that the correlation matrix is given by

$$D_{ij} = E[(u_i(x,t)-u_i(y,t))(u_j(x,t)-u_j(y,t))] = S_2(r,t)I + (S_2(r,t)-S_2(q,t))\frac{r_i r_j}{r^2},$$

where I is the identity matrix in $\mathbb{R}^3 \times \mathbb{R}^3$, and

$$S_2(q,t) = S_2(r,t) + r\frac{\partial}{\partial r}S_2(r,t),$$

with $r = |r|$, $|\cdot|$ denoting the vector norm in $\mathbb{R}^3$. For $\eta << r$, D_{ij} is expected to reduce to

$$D_{ij} = C_2(\varepsilon r)^{2/3}(\frac{4}{3}I - \frac{1}{3}\frac{r_i r_j}{r^2}).$$

Thus in $\mathbb{R}^3$ the correlation matrix is determined by longitudinal structure function alone and we will restrict our attention to them.

Consider the longitudinal third-order structure function above,

$$S_3(r,t) = \frac{8}{C^3}\sum_{k\in\mathbb{Z}^3}\Big[(|\sin^3(\pi k\cdot r)|)\Big\{\frac{\frac{C}{2}c_k|d_k|(1-e^{-2\lambda_k t})(1-e^{-\lambda_k t})}{|k|^{\zeta_3}+\frac{8\pi^2\nu}{C}|k|^{\zeta_3+\frac{4}{3}}+\frac{16\pi^4\nu^2}{C^2}|k|^{\zeta_3+\frac{8}{3}}} + \frac{|d_k|^3(1-e^{-\lambda_k t})^3}{|k|^{\zeta_3}+\frac{12\pi^2\nu}{C}|k|^{\zeta_3+\frac{4}{3}}+\frac{48\pi^4\nu^2}{C^2}|k|^{\zeta_3+\frac{8}{3}}+\frac{64\pi^6\nu^3}{C^3}|k|^{\zeta_3+4}}\Big\}\Big],$$

where $c_k = c_1 + c_2 + c_2$, $|d_k| = \sqrt{d_1^2+d_2^2+d_2^2}$ and $|k| = \sqrt{k_1^2+k_2^2+k_2^2}$, and $r = x - y$. If we take $r = (r,0,0)$ to lie along the axis of the VDTT (cylinder), then $r\cdot k = (rk_1,0,0)$ and if we ignore k_2 and k_3 in the denominator of S_2, and take $t\to\infty$, we get the inequality

$$S_3(r,t) \le \frac{8}{C^3}\sum_{k_1\neq 0}\Big[(|\sin^3(\pi k_1 r)|)\Big\{\frac{\frac{C}{2}\tilde{c}_{k_1}|\tilde{d}_{k_1}|}{|k_1|^{\zeta_3}+\frac{8\pi^2\nu}{C}|k_1|^{\zeta_3+\frac{4}{3}}+\frac{16\pi^4\nu^2}{C^2}|k_1|^{\zeta_3+\frac{8}{3}}} + \frac{|\tilde{d}_{k_1}|^3}{|k_1|^{\zeta_3}+\frac{12\pi^2\nu}{C}|k_1|^{\zeta_3+\frac{4}{3}}+\frac{48\pi^4\nu^2}{C^2}|k_1|^{\zeta_3+\frac{8}{3}}+\frac{64\pi^6\nu^3}{C^3}|k_1|^{\zeta_3+4}}\Big\}\Big],$$

because $\zeta_3 = 1$, where $\tilde{c}_{k_1} = \sum_{k_2\neq 0}\sum_{k_3\neq 0} c_{(k_1,k_2,k_3)}$, $|\tilde{d}_{k_1}| = \sum_{k_2\neq 0}\sum_{k_3\neq 0}|d_{(k_1,k_2,k_3)}|$. We have used the convexity of the functions $f(x) = x^p,\ p\ge 1$ to take the sum into the powers, here $p = 1,3$. This upper estimate, that is supposed to be close, reduces the three dimensional S_3 to the one dimensional one. The argument for all the structure functions $S_p,\ p\ge 3$, is similar but the argument does not hold for $p = 1$, or 2, because $\zeta_1 = 0.37$ and $\zeta_2 = 0.696$ so both are less than one. This means that the upper estimate does not hold for all $|k|$s, only the ones that are big enough so that the second term in the denominators of S_1 and S_2 dominates the first. We will use the upper estimate with this understanding. We will compare the one dimensional structure function with experimental data and drop the subscript 1 on k_1. Thus the general p-th

one-dimensional longitudinal structure function, in the stationary state, is given by

$$S_p(r,t) \leq \frac{2^p}{C^p} \sum_{k\neq 0} \frac{2^{\frac{p}{2}}\Gamma(\frac{p+1}{2})\sigma_k^p {}_1F_1(-\frac{1}{2}p, \frac{1}{2}, -\frac{1}{2}(\frac{M_k}{\sigma_k})^2)}{|k|^{\zeta_p} + \frac{p_k\pi^2\nu}{C}|k|^{\zeta_p+\frac{4}{3}} + O(\nu^2)} |\sin^p[\pi k r]|, \tag{2.17}$$

where Γ is the gamma function, ${}_1F_1$ is the hypergeometric function, $M_k = |\tilde{d}_k|$, $\sigma_k^2 = \frac{C}{2}\tilde{c}_k$, and p_k is different for each denominator term in the series. Note that the Taylor-Reynolds number dependence is captured via the viscosity term ν. C is a constant approximating the mean velocity fluctuation of the flow. The upper estimate is understood to hold for $p = 1,2$ when $|k|$ is large enough.

We can think about the triple sum as an integral

$$\sum_{k\in\mathbb{Z}^3\setminus\{0\}} c_k \sim \int_0^\infty \int_\omega c_k d\omega |k|^2 d|k| = \int_0^\infty \tilde{c}_k dk \sim \sum_{k\neq 0} \tilde{c}_k,$$

where $|k|$ is the radius of the three-vector k. This means that

$$\tilde{c}_k = \int_\omega c_k d\omega |k|^2,$$

is the integral of c_k over a sphere of radius k is Fourier space, analogous to the energy shell in the Kolmogorov-Obukhov cascade. Thus, whereas $c_k \sim \frac{1}{k^{3+\varepsilon}}$, where $k = |k|$, in order for the sum to converge, $\tilde{c}_k \sim \frac{1}{k^{1+\varepsilon}}$. A similar argument applies to $\sum_{k\in\mathbb{Z}^3\setminus\{0\}} |d_k|$ For this reason we expect the exponent m of k below to satisfy $m > 1$. We will in fact make the ansatz,

$$\tilde{c}_k = \sqrt{\frac{2}{\pi}}\frac{b}{b^2+k^m},\ \tilde{d}_k = \sqrt{\frac{2}{\pi}}\frac{a}{a^2+k^m}, \tag{2.18}$$

where $\tilde{c}_k$ and $\tilde{d}_k$ are the one-dimensional versions of the coefficients in the structure functions, to approximate the experimental data. Provided that m is greater than 1, the series determining the one dimensional restriction of the structure functions (2.17) will converge. The $\sqrt{\frac{2}{\pi}}$ factor in both formulas is placed there to compensate for the Fourier Transform operation in Mathematica. The thinking here is that there is a universal coefficient m for each Reynolds number that will determine how fast the sine series converges, and thus the spatial smoothness

of the structure functions. Thus for k large, $\tilde{c}_k$ and $\tilde{d}_k \sim \frac{1}{k^m}$. Moreover, we are (optimistically) assuming that the two contributions $\tilde{c}_k$ and $\tilde{d}_k$, to the large eddies, also scale with the order of the structure functions and can be characterized by a number b, respectively a, for each Taylor-Reynolds number. Thus for k small, $\tilde{c}_k \sim \frac{1}{b}$ and $\tilde{d}_k \sim \frac{1}{a}$. This turns out to work reasonably well, see Table 5.

In summary, we are able to reduce the three-dimensional coefficients c_k and d_k to the one-dimensional coefficients $\tilde{c}_k$ and $\tilde{d}_k$, respectively, and so use the one-dimensional formulas to fit to the data, and formulate a simple ansatz (2.18), for coefficient's dependance on the Taylor-Reynolds number and the wavenumber $1/k$.

Chapter 3

Wind-Tunnel Generated Homogeneous Turbulence

3.1 History of Wind Tunnel Experimentation

In Aeronautics the design of airfoils and airplanes was originally a major challenge. There was a lack of experiments designed and performed under laboratory conditions and this hampered progress. The development of the wind tunnel turned out to be the major breakthrough in creating the necessary experiments. The first wind tunnel is credited to F. Wenham in Great Britain in 1871, the Wright brother also made their own wind tunnel in 1901 [22], but it was Ludwig Prandtl in 1917 who designed the first "modern" wind tunnel. This wind tunnel was actually his second design. In 1909, he designed the first closed-loop wind tunnel, but it was, by his own admission, "of a temporary nature" [23]. Thus, a more permanent design was made which would become the foundation for all subsequent wind tunnels [24]. Prandtl's student, Max Munk, would go on to design the first wind tunnel which allowed an adjustment of the density of the working fluid [2], allowing for a much higher Reynolds number flow in the tunnel. This tunnel was built in at the Langley Research Center in Virgina in 1923. However, most

of the research done by Prandtl and others working with wind tunnels was devoted to studying airfoils and airplane shapes [2].

In addition to being the perfect tool to study airfoils and model airplanes, wind tunnels are suitable for the creation of statistically homogeneous and isotropic turbulence, see Taylor [25], in an experimental setting. Such a flow limits turbulence to its essential ingredients: inertia, pressure and friction. It also minimizes the effects of the boundaries on the flow and does not exhibit a preferred orientation. It can be created by mechanically stirring a liquid or gas [2]. A close approximation of such flows are realized in a wind tunnel when a uniform free-stream flow is disturbed by a mesh or a grid, see [26, 27].

Experiments performed to study homogeneous or more general turbulence were rare until the second half of the twenthieth century. The 1940s featured experiments on grid turbulence in California [28], while another series of experiments were performed at the Nuclear Research Lab in Jülich in the 1970s [29]. More recently, wind tunnels were built at the German Aerospace Center in Göttingen and at the Princeton Gas Dynamics Lab with the goal of studying turbulence. The facility where the experiments in this dissertation where performed, the Variable Density Turbulence Tunnel (VDTT) at the Max Planck Institute for Dynamics and Self-Organization in Göttingen, was completed in 2009, see [2]. It has achieved turbulent flow up to Taylor-Reynolds number 1600, which is the highest recorded for a grid experiment. Details about the VDTT can be found in [2]. One of Prandtl's original wind tunnels sits besides the VDTT in Göttingen, see [2].

In this dissertation, we will examine the structure functions of turbulence coming from data obtained in the VDTT. We will compare with the stochastic closure theory in [9] and show that the Reynolds number dependence of the data is captured by this theory, which was originally published in [1]. More surprisingly, we obtain unexpected results on the smoothness of the flow velocity, in homogenous turbulence, from the data.

3.2 Comparison of the Model with the Data

The data in this chapter was obtained from the Max Planck Institute for Dynamical and Orgranization, located in Göttingen, Germany and was generated by the Variable Density Turbulence Tunnel (VDTT). The pressurized gases circulate in the VDTT in an upright, closed loop. At the upstream end of two test sections, the free stream is disturbed mechanically. The data in the current chapter is generated by a fixed grid. However, the gas stream can also be disturbed by an active grid resulting in even higher Reynolds number turbulence. In the wake of the grid the resulting turbulence evolves down the length of the tunnel without the center region being substantially influenced by the walls of the tunnel, see [2]. The measurements were performed with a Dantec StreamLine hot wire anemometry system, see [2].

The measurements were taken at fifty logarithmically placed distances ranging from 1.5 to 8.3m downstream from a classical grid. For more information about the experiment, see [30]. The longitudinal differences are

$$\delta u(x,r) = u(y,t) - u(x,t) = u(x+r,t) - u(x,t)$$

where u, x and r are parallel vectors (along the x-axis). Taylor's frozen flow hypothesis is used to extract x and r from the time series of the probe, see [2]. The test sections are about 8 meters long, long enough for the turbulence to evolve through at least one eddy turnover time, around 1 second, see [2]. This means that the turbulence can be observed over the time that it takes the energy to cascade all the way from the large eddies to the dissipate scale. More details about the tunnel can be found in [2].

Measurements were taken for Taylor Reynolds Numbers 110, 264, 508, 1000, and 1450. The pertinent parameters for the data are given Table 1. The system length in the tunnel is an important value for fitting the data because we have to scale the lag variable r, $\frac{r/\eta}{\text{system length}} = (x-y)$, with the system length. One might think that the system length is the square root of the cross sectional value of the tunnel $\sqrt{A}$, but in fact the relevant system length is the grid size of

Taylor Reynolds Number	η	L	ν
110	1025	165.1	0.0000155
264	162	102.5	0.00000234
508	91	123.9	0.00000100
1000	36	136.6	0.000000291
1450	22	129.5	0.000000150

Table 3.1: Here, η is the Kolmogorv length scale given in micrometers, L is the Taylor length scale given in millimeters, and ν is the viscosity given in $\frac{m^2}{s}$.

the grid used to perturb the gas flow upstream from the measurement section. This raises the question whether the grid size influences the shape of the largest eddies in the flow and we will see below that the answer is yes, it does so for the smaller Reynolds numbers. For the larger Reynolds numbers this influence disappears, see Table 5.

The structure function were plotted against $\frac{r}{\eta}$, where r is the distance between positions x and y as given by the Taylor Frozen Flow Hypothesis and η is the Kolmogorov length scale. The final recorded data point occurs at $\frac{r}{\eta} = 19540$. Thus, we substitute $\frac{r}{\eta}/(19540(D))$ for $x-y$, where D is an constant greater than 1, in the above formulas. This is done to compensate for the system length of each measurement. We assume periodic boundary conditions in the Navier Stokes equation (2.1) and (2.6). Thus, we divide $\frac{r}{\eta}$ by $19540(D)$ so that our sine series formula will capture the entire data set. Once found, D, the system length, is fixed for a particular Taylor Reynolds number across the varying structure functions. The found values for D are given in Table 5.

Fitting was done in Mathematica using the internal FindFit command. An example of the code for Reynolds Number 110 is given in Appendix A. Due to computational time, the series given in Chapter 2 was run out to one thousand terms. Initial fitting to the formulas given in Chapter 2 proved to not be effective. It was assumed that the largest eddies were influenced by the active grid in the wind tunnel and thus, were influencing the fitting routine. Thus, to

Re Lambda	110	264	508	1000	1450
Second	0.00744	0.0153	0.0169	0.0183	0.0195
Third	0.00154	0.00162	0.00484	0.00564	0.00664
Fourth	0.000384	0.00189	0.00228	0.00251	0.00305
Sixth	0.0000341	0.000431	0.000566	0.000552	0.000691
Eighth	$3.12(10^{-6})$	0.0000839	0.000122	0.000144	0.000204

Table 3.2: The fitted values for A_1 in equation (3.1).

Re Lambda	110	264	508	1000	1450
Second	0.00285	0.00583	0.00653	0.00697	0.00666
Third	0.000872	0.00124	0.00526	0.00488	0.00395
Fourth	0.000174	0.000746	0.000804	0.00100	0.000600
Sixth	$4.24(10^{-6})$	-0.0000756	-0.00011	0.0000919	0.0000654
Eighth	$1.04(10^{-6})$	0.0000127	0.0000147	0.0000264	$-4.71(10^{-7})$

Table 3.3: The fitted values for A_2 in equation (3.1).

compensate, we do not tie the first two sine terms to formula given in (2.16). Instead, we allow them to have free coefficients. In other words, the new model used to fit the data is given by

$$A_1|\sin[(\pi\times r)/(19540.3(D))]|+A_2|\sin^2[(2\pi\times r)/(19540.3(D))]| + \sum_{k=3}\frac{2^p}{C^p}A_p|\sin^p[\pi k\cdot(x-y)]|, \tag{3.1}$$

where A_p is still given by (2.16) This was done for all structure function fits. Experimentation found that the best result came from using the fourth structure function for each Taylor Reynolds Number to fix the coefficients a, b, and D. This is likely the result of the Fourth Structure Function being the largest structure function still bound by the Sobolev inequality, see Section 3.6.

Tables 2, 3, and 4 contain the found values for A_1, A_2 and C respectively, as described in (3.1).

Taylor Reynolds Number	110	264	508	1000	1450
Second	2.8	3.31	4.21	7.62	21.1
Third	1.4	1.93	1.49	2.72	3.59
Fourth	1.07	1.01	1.19	2.36	6
Sixth	1.15	1.29	1.34	1.73	2.49
Eighth	0.616	0.531	0.596	1.17	2.84

Table 3.4: The fitted values for C in eq. (3.1)

Taylor Reynolds Number	a	b	D
110	11.64	0.01612	1.569
264	9.581	0.05236	1.769
508	8.314	0.06504	1.518
1000	3.792	0.09247	1.32
1450	2.684	0.4092	1.3

Table 3.5: The fitted values for a, b, and D in eq. (2.17)

Taylor Reynolds Number	110	264	508	1000	1450
Second	**1.563**	**1.16**	**1.069**	0.8965	0.9148
Third	**1.408**	**1.185**	0.922	0.6488	0.5262
Fourth	**1.269**	0.8751	0.7936	0.5554	0.4865
Sixth	0.98607	0.5055	0.5192	0.4339	0.3398
Eighth	0.9711	0.5924	0.5755	0.3771	0.2482

Table 3.6: The fitted values for m in eq. (2.17. Note that the numbers in bold are greater than one.)

3.3 Evaluation of the Model

The fitting results can be found in figures A.1-A.26. The blue diamonds are the data points while the red line is our fitted function. All the plots are on a log-log scale except for a single plot of the third structure function at Taylor Reynolds Number 110. This is included for perspective. We see that the fitting is good for most of the structure function for most of the Reynolds numbers. There are little wiggles at the largest scales (largest values of the lag variable). This is presumably related to the interaction between the large and small eddies, which is magnified for the sixth and eighth-order structure functions by the smoothness of the flow, described below. At the highest Reynolds numbers and highest order (sixth and eighth) structure functions, we see a divergence at the smallest scales (smallest values of the lag variable). This is indicative of the divergence of the series for these structure functions at the highest Reynolds numbers. In general, we note that the fits become less accurate as we increase the structure function number. The fits for the second, third, and fourth structure functions are generally quite good but the sixth and eighth structure function fits are rougher, at the higher Reynolds numbers. This is expected from the theory given by in [9], see below.

Table 5 gives the fitted values for a and b. This table shows that the Central Limit Theorem term as given by b has a greater influence for smaller Taylor Reynolds numbers than the Large Deviation Principle term, given by a, as for small values of k, these terms essentially become $\frac{1}{a^2}$ and b, respectively, because b is small. As the Reynolds number goes up, we do see an increasing influence of b dominating the increase of $\frac{1}{a^2}$, see the plot in Figure A.29. Thus the contribution of the Central Limit Theorem is greater. The influence of the grid on the lowest Fourier modes A_1 and A_2 is plotted in Tables 2 and 3. These contributions are small for low order structure functions and become insignificant for the higher order structure functions, for all Reynolds numbers. Thus the influence of the grid on large eddies is small and becomes negligible for the higher structure functions.

The values of the exponent m of the wavenumber $k = k_1$ are given in Table 6. In general the exponents are larger or very close to 1, towards the top of the table. The first (top) line in Table 6, corresponding to the second order structure function, verifies the hypothesis on the coefficients c_k and d_k in Chapter 2. The energy shell coefficient $\tilde{c}_k$ and $\tilde{d}_k$ should decay as $|k|^{-m}$, $m > 1$. All the exponents in the first line in Table 6 satisfy this except the last two. However, both still lie within the fitting uncertainty and may be explained by the Reynolds number corrections absorbing the weight of the power. Thus the exponents $m(R_\lambda)$ in the first line depend on R_λ, but approach 1 as R_λ becomes large. We would expect the exponents to remain above one for the rest of the lines on the table, but this is not the case. This results gives us insight into the smoothness of the flow, as explained below.

3.4 The Improved SCT Model

The comparison of theory and data for homogeneous turbulence now produces a much improved Stochastic Closure Model, removing the infinitely many coefficients c_k, d_k and h_k from Equation (2.6). Namely, the large scale satisfy the equation (2.3) whereas the small scale flow satisfies the stochastic Navier-Stokes equation,

$$\begin{aligned} du + u\cdot\nabla u dt = {} & [\nu\Delta u + \nabla(\Delta^{-1}[\mathrm{Trace}(\nabla u)]) - u\cdot\nabla U - U\cdot\nabla u]dt \\ & + \sum_{k\neq 0}\left(\frac{a}{|a|^2+|k|^m}\right)|k|^{-\frac{5}{3}} dt e_k(x) + \sum_{k\neq 0}\frac{b^{1/2}}{(|b|^2+|k|^m)^{1/2}}|k|^{-1} db_t^k e_k(x) \\ & - u(\frac{1}{3}\sum_{k\neq 0}\bar{N}_t^k dt), \end{aligned} \tag{3.2}$$

where $a, b^{1/2} \in \mathbb{R}^3$. Here $k \in \mathbb{R}^3$ also and $e_k(x) = e^{2\pi k\cdot x}$. The SCT model now depends on only three parameters $a = |a|$, $b = |b|$ and m that are all function of the Taylor-Reynolds number R_λ. A plot of a and b from Table 5 are shown in Figure A.28. It shows that the Large Deviation coefficient a is larger than the Central Limit Theorem coefficient b. But this is deceiving

because the right comparison is between $1/a^2$ and b for small wavenumber k, because of the form of the coefficients c_k, d_k in (2.18). This comparison is shown in Figure A.29. We see that b is larger than $1/a^2$ and dominates for large Reynolds numbers. For large wavenumbers k, b dominates even more because now it is compared with a^2/k^2. The conclusion is that the Central Limit Theorem term is the main contributor to the noise and the bias given by the Large Deviation term is only significant for small wavenumbers k and small Reynolds numbers.

The coefficient C that appears in the computation of the structure functions (2.17) is not constant for each Taylor-Reynolds number, see Table 4, because it measures both the size of the velocity fluctuations and the relative strength of the Center Limit Theorem term and the Large Deviation term in the noise. However, it does not vary much over the center part of Table 4 as a function of the Taylor-Reynolds number. The exponent m also varies because some of the correction terms in (2.17) absorb its weight and because of the smoothness issue for the higher order structure functions that is discussed below. However, it also does not vary much with the Taylor-Reynolds number above the diagonal, as signified by the bolded numbers, in Table 6.

3.5 Sensitivity Analysis

We now consider the formula for the general p-th structure function as given in (2.17). If we let the viscosity of the fluid head to zero, the Reynolds Number will go to infinity. This will simplify the coefficients A_p in (2.17), for $R_\lambda = \infty$, $\nu = 0$,

$$A_p = \frac{2^{\frac{p}{2}}\Gamma(\frac{p+1}{2})\sigma_{k1}^p F_1(-\frac{1}{2}p, \frac{1}{2}, -\frac{1}{2}(\frac{M_k}{\sigma_k})^2)}{|k|^{\zeta_p}}. \tag{3.3}$$

The further denominator terms found in (2.17) but not above, are corrections to the formula to account for the Reynolds number of the flow. Data fits were also done to the formula without the Reynolds number corrections. Figures A.35-A.59 are plots of the error between the formula

fits and the data at each data point. Here, error is defined at each data point to be the absolute value of the difference between the data points and the model. The blue circles are the error to the Reynolds corrected formulas while the red diamonds are the error to the formula without the Reynolds number correction.

There are a couple of observations to make about the error plot. First, for small Taylor Reynolds numbers, it appears that the corrections improve the fitting, especially for the smaller data points. This improvement erodes as the Taylor Reynolds number increases, until we see very little difference in accuracy for Taylor Reynolds number 1450. This makes sense, as the corrections to account for Reynolds number get smaller as the Reynolds number increases, with the formulas becoming the uncorrected version when we let the Reynolds number go to infinity.

A second observation may also help explain the issue surrounding the m values of the second order structure functions for high Reynolds numbers, discussed in detail below. Table 7 contains the found values for m without the Reynolds number corrections. Here we see a diagonal much more in line with what the SCT predicts. Notice that the Reynolds correction adds the terms

$$\frac{p_k \pi^2 \nu}{C} |k|^{\zeta_p + \frac{4}{3}} + O(\nu^2),$$

to the denominator of the fractions. In particular, this is adding higher powers of k, which may be absorbing some of the power of m, which explains why we see a much more pronounced diagonal form with the exponents when looking at the uncorrected version of the formula in Table 7 than in Table 6 with the corrected version of the formulas.

Finally, we also see an issue in fitting the smallest data points for Reynolds Number 1450. This issue appears to be connected to the system length, as seen in Figure A.27. A second fit to the fourth structure function was found with $D = .921$. This does improve the fitting for the smaller data points. However, D being this small causes an issue at the larger data

Taylor Reynolds Number	110	264	508	1000	1450
Second	**2.09081**	**1.49402**	**1.31448**	**1.07963**	0.984291
Third	**1.79012**	**1.41339**	**1.05553**	0.822192	0.730565
Fourth	**1.6408**	**1.09179**	0.920749	0.687336	0.595942
Sixth	**1.65727**	**1.08667**	0.91658	0.681818	0.592901
Eighth	**1.66164**	**1.06728**	0.901549	0.662111	0.577724

Table 3.7: The fitted values for m for the uncorrected for Reynolds number effects structure function fits

points, namely the sine curve wants to return to zero before the last data point. Since there are relatively few data points at small values of $\frac{r}{\eta}$, we set $D = 1.3$. The value of 1.3 was chosen as it the smallest number needed to fully capture the larger data points.

One potential point of concern with the fitting result was the probe size. The size of the probe could influence the fit and a different probe size could produce different result. To check for this, fits were redone with a reduced number of data points. In particular, for every Taylor Reynolds number and every structure function, fits were redone without including the first, the first two, and the first three data points respectively. We saw minimal change in the main parameters. the greatest being a difference of one in the third significant digit. The robustness test for Reynolds Number 508 are included in Figures A.30-A.34. As we can see, there is not a significant change in the value of m when removing the first couple of data points. We do see significant changes as more data points are removed. However, the removal of fifteen or more data points removes the entire dissipative range and so we would expect the changes to be significant. As a result, we are convinced the fits are unaffected by the probe size.

3.6 The Smoothness of the Velocity

It was pointed out by Onsager [31, 32] that the fluid velocity in fully turbulent flow could not be a spatially smooth function, in the limit of infinite Taylor-Reynolds number.

The last line in Table 6, corresponding to the eighth order structure function, tells an interesting story, that was totally unexpected. There only the exponent for the smallest Reynolds number is close to one. All the other exponents are well below one, the one for the highest Reynolds number going down to 0.248. This seems to contradict the fits for the exponent m from the first line in the Table and the hypothesis on coefficients c_k and d_k. In fact, there is a "diagonal" in Table 6, below which the coefficient are well below one, and above which they are larger than one within the fitting uncertainty. The resolution of this apparent contradiction is that the structure functions below the diagonal are not finite in the limit of a very large large Taylor-Reynolds number R_λ and the series (2.15) representing them do not converge as $R_\lambda \to \infty$. This is what the fits show. To explain this we have to discuss the L^p and Sobolev function spaces and the Sobolev inequality, that relates the existence of moments of velocity differences to the differentiability (smoothness) of the turbulent fluid velocity. To check this, we need the Sobolev Inequality:

Theorem 3.6.1 *The Sobolev Inequality: Assume $f \in H^k(\mathbb{T}^3)$. Then, $f \in L^q(\mathbb{T}^3)$, where*

$$\frac{1}{q} = \frac{1}{2} - \frac{k}{3},$$

and we get the inequality

$$|f|_{L^p} \leq C\|f\|_{H^n}.$$

For our purposes, the Sobolev inequality can be written as

$$|u|_p \leq C\|u\|_n$$

where $n \geq \frac{3}{2} - \frac{3}{p}$, in three dimensions, and C is a constant. It says that the nth Sobolev space of functions with n derivatives in L^2,

$$\|u\|_n = \sqrt{\sum_{j=0}^{n} |\nabla^j u|_2^2}$$

lies in the space of functions, whose pth moment

$$|u|_p = \left(\int_{\mathbb{R}}^{2} |u|^p dx \right)^{1/p} < \infty$$

is finite. Thus in order for the pth moment (power) of a function to be finite, it is sufficient that it has n derivatives . We apply the Sobolev inequality to the gradient of u below, in order to compare with the moments of the velocity differences δu.

In [9], using Onsager's observation, Birnir showed that the velocity, u, must lie in Sobolev space H^n, where $n = \frac{11}{6}$, when intermittency is not taken into account and $n = \frac{29}{18}$ when it is. This, in turn, implies that ∇u lies in Sobolev space H^n, where $n = \frac{5}{6}$ without intermittency and $n = \frac{11}{18}$ with intermittency. In order to guarantee convergence of the sine series, we need $H^n \subset L^p$, where p is the number of the structure function. To check this, we need the Sobolev Inequality:

Theorem 3.6.2 *The Sobolev Inequality: Assume $f \in H^k(\mathbb{T}^3)$. Then, $f \in L^q(\mathbb{T}^3)$, where*

$$\frac{1}{q} = \frac{1}{2} - \frac{k}{3},$$

and we get the inequality

$$\|f\|_{L^q} \leq C \|f\|_{H^k}.$$

Thus, we get convergence of the Sine series provided that

$$|\nabla u|_p \leq C \|\nabla u\|_n,$$

where C is a constant and $\|\cdot\|_n$ denotes the Sobolev norm, or

$$\frac{5}{6} \geq \frac{3}{2} - \frac{3}{p}.$$

This is true for $p=2$, $p=3$ and $p=4$, but does not hold for $p=6$ and $p=8$. Now approximate the velocity differences by the gradient $\delta u \sim \nabla u \cdot r$. Hence, the increase in roughness for the sixth and eighth structure functions agrees with the theory presented by Birnir in [9].

A second issue, indicative of intermittency, arose during the fitting process for the values for m for Taylor Reynolds number 1000 and 1450, see Table 7, where the Taylor-Reynolds number dependence of the structure function has been removed. This prevents the correction terms from absorbing the weight of the exponent m. We mentioned before that m needs to be greater than one in order to ensure convergence. We expect this might not hold for structure functions six and eight for the same reason given in the previous paragraph. However, we get a value less than one for the third and fourth structure functions for Reynolds number 1000 and 1450. While this is by no means a conclusive proof, it may be suggestive of an increasing influence of intermittency as the Reynolds number increases. The inequality $\frac{5}{6} \geq \frac{3}{2} - \frac{3}{p}$ above does not take into account the influence of intermittency. The new inequality when taking intermittency into consideration is

$$\frac{11}{18} \geq \frac{3}{2} - \frac{3}{p}.$$

Now, this is only true $p=2$ and $p=3$, but not for $p=4,6,8$, and $p=3$ is close to the borderline. Hence, the divergence of the series, for the third and fourth structure functions for Taylor Reynolds number 1000 and 1450, may point to an *increasing influence of intermittency* causing a further loss of smoothness in the flow.

The argument for the non-smoothness of the velocity as indicated by the data is following. We have seen that the theory produces the measured structure functions for small Reynolds numbers and order of structure function less than or equal to eight. This lets us conclude that the formulas for the structure functions are correct and should give the right values for all orders and all Reynolds numbers. In Table 7, we see that for large Reynolds numbers, 1000 and 1450, the sixth and eight structure functions are given by a series that does not converge, if

it was summed for all k, because $m < 1$ within the measurement accuracy. Thus for higher and higher Reynolds number the sixth and the eight structure functions increase without bound and become infinite in the limit of infinite Reynolds numbers. In distinction, the structure function of order three or less are finite for all Reynolds numbers.

Chapter 4

Townsend-Perry Constants and Wall Turbulence

4.1 History of Turbulent Boundary Layer Analysis

Turbulence resulting from a boundary layer appears a great deal in nature and in engineering applications. In comparison to the homogeneous turbulence generated from the wind tunnel, turbulent boundary layers are marked by the interaction of inertia with the boundary. Recent investigations into turbulent boundary layers have focused on the logarithmic dependence of the second-order moment u', the streamwise velocity fluctuation. This logarithmic dependence was first by Townsend, see [33], and then developed by Perry *et al.*, see [34] and [35]. Recently, Meneveau and Marusic have extended this logarithmic scaling to higher-order moments of u', see [36]. They also noted a sub-Gaussian behavior to the scaling, a characteristc which we seek to explain using the SCT.

In [33], Townsend theorized the logarimthmic dependence of the second-order moment u' by generalizing the Prandtl-von Kármán law of the wall to the velocity fluctuations. This

dependence was then developed by Perry, see [34] and [35], as

$$\frac{\langle (u')^2 \rangle}{u_\tau^2} = \langle (u'^+)^2 \rangle = B_1 - \alpha_1 \ln(\frac{y}{\delta}). \tag{4.1}$$

Here, $\langle \cdot \rangle$ denotes time and $x-z$ space ensemble averaged, $u' = u - \langle u \rangle$, $\delta = \delta_{99}$ is the boundary thickness, and the superscript $+$ indicates normalization using the friction velocity $u_\tau = \sqrt{\frac{\tau_0}{\rho}}$, where τ_0 is the mean stress at the wall and ρ is the density. Note that we use α_1 instead of the standard A_1 here to avoid confusion with the earlier use of A_p. This formulation was then generalized to higher-order moments by Meneveau and Marusic in [36], based on an analogy to the Gaussian, to give the generalized logarithmic law

$$\langle (u'^+)^{2p} \rangle^{\frac{1}{p}} = B_p - \alpha_p \ln(\frac{y}{\delta}) = D_p(\mathrm{Re}_\tau) - \alpha_p \ln(y^+), \tag{4.2}$$

where $y^+ = \frac{y u_\tau}{\nu}$ is the viscous unit and $D_p = B_p + \alpha_p \ln(\mathrm{Re}_\tau)$ is a Reynolds number dependent offset. Here, $\mathrm{Re}_\tau = \frac{\delta u_\tau}{\nu}$. These α_p are called the generalized Townsend-Perry constants, see [37] and [38].

4.2 The Data

The data considered here was generated at the University of New Hampshire in the flow physics facility (FPF). The FPF draws from the atmosphere and generats flow speed using two vane-axial fans. Measurements were then taken in the boundary layer that develops along the floor of the FPF. The pertanent information for the data is given in Table 4.1.

Marusic in [36] defined the logarithmic region to lie $400 < y^+ < 0.3 \times \mathrm{Re}$. However, we follow the work of Klewicki *et al.* in [39] and search for the logarithmic behavior in the region $2.6\sqrt{\mathrm{Re}} < y^+ < 0.3 \times \mathrm{Re}$. Table 4.2 gives the values of α_p at each of the above Reynolds number for $p \leq 6$.

Reynolds Number	$u_\tau(m/s)$	$\delta_{99}(m)$	$\nu(m^2/s)$
1450	0.263	0.0861	1.562×10^{-5}
2180	0.252	0.1356	1.568×10^{-5}
3820	0.24	0.2456	1.505×10^{-5}
6430	0.234	0.4284	1.559×10^{-5}
10770	0.226	0.7363	1.545×10^{-5}
15740	0.33	0.7171	1.503×10^{-5}
19670	0.432	0.6885	1.512×10^{-5}

Table 4.1: Here, $u_\tau = \sqrt{\frac{\tau_w}{\rho}}$ is the friction velocity, where τ_w is the mean wall shear stress and ρ is the mass density, δ_{99} is the boundary layer thickness, and ν is the kinematic viscosity

Reynolds Number	1	2	3	4	5	6
1450	0.8248	1.3277	1.7625	2.1402	2.4667	2.738
2180	0.7758	1.2273	1.6226	1.983	2.3379	2.7377
3820	0.978	1.5298	1.9861	2.3712	2.7095	3.028
6430	1.2035	1.8643	2.4304	2.931	3.3849	3.8108
10770	1.2831	2.0048	2.5792	3.04	3.4283	3.7852
15740	1.1967	1.8609	2.3956	2.8228	3.162	3.4323
19670	1.3449	2.1307	2.7982	3.3735	3.886	4.3689

Table 4.2: The values of α_p for $p = 1,2,3,4,5,6$ at each Reynolds number

4.3 The Model

To show how the SCT can be applied to the Townsend-Perry constants, we follow the work of Birnir and Chen in [10]. The logarithmic behavior is based on the Attached Eddy Hypothesis. We can use the Fluctuation Similarity Hypothesis to formulate the generalized log law. We start by considering turbulent eddies with streamwise characteristic size l. The velocity difference is then given by

$$\delta u = \frac{|u(x+l,y-u(x,y)|}{l}.$$

Using dimensional analysis, we can then define the streamwise shear stress to be

$$\tau_\star = \frac{\nu|u(x+l,y)-u(x,y)|}{l}. \tag{4.3}$$

Finally, we can define $u_\star = \sqrt{\tau_\star}$ in analogy to the friction velocity. While $u_\star$ is different from u', they are both Galilean invariant velocities and the result of the motion of turbulent eddies. Hence, we introduce the similarity hypothesis to give

$$\frac{\langle (u')^{2p}\rangle^{\frac{1}{p}}}{\langle (u')^2\rangle} = \frac{\langle u_\star^{2p}\rangle^{\frac{1}{p}}}{\langle u_\star^2\rangle}. \tag{4.4}$$

Then, by plugging 4.1 into 4.4, we get

$$\frac{\alpha_p}{\alpha_1} = \frac{\langle u_\star^{2p}\rangle^{\frac{1}{p}}}{\langle u_\star^2\rangle}. \tag{4.5}$$

Now, in [10], Birnir and Chen derived further the formula

$$\frac{\alpha_p}{\alpha_1} = (l^\star)^{\frac{\zeta_p}{p}-\zeta_1}\frac{C_p^{\frac{1}{p}}}{C_1}, \tag{4.6}$$

where C_p are the A_p defined in 2.16 in Chapter 2, and showed excellent agreement with data generated by Marusic.

Unfortunately, this formula did not provide agreement with the data generated by Klewicki. The reason for this is the compensation by C_1. As can be seen in formula 2.12, the first structure

Reynolds Number	a	b	m	C
1450	13.380	3.461×10^{-7}	1.714	4.967
2180	13.176	8.400×10^{-7}	1.669	3.962
3820	12.836	2.931×10^{-6}	1.600	2.950
6430	12.501	8.172×10^{-6}	1.539	2.240
10770	12.082	2.415×10^{-5}	1.469	1.718
15740	12.081	2.421×10^{-5}	1.469	1.741
19670	12.120	2.208×10^{-5}	1.475	1.776

Table 4.3: The interpolated values for the parameters a, b, m, and C in equation 2.6

function does not contain a Central Limit Theorem term, which proves to be the more important term for fitting. Instead, we compensate by $C_2^{\frac{1}{2}}$. Hence, we fit to the formula

$$\frac{\alpha_p}{\alpha_1} = (l^\star)^{\frac{\zeta_{p+1}}{p+1}-\frac{\zeta_2}{2}} \frac{C_{p+1}^{\frac{1}{p+1}}}{C_2^{\frac{1}{2}}}. \tag{4.7}$$

4.4 Computing C_p

Unfortunately, while the data sets from New Hampshire were run long enough to compute the α_p, they were not run long enough for the streamwise structure functions to converge. Thus, there was no way to determine the parameters a, b, m, and C directly from the data, and so the parameters were found by interpolating the parameters found in Chapter 3 from the Göttingen data. The assumption here is that, in the inertial layer, the flow in the streamwise direction is roughly homogeneous. Table 4.3 gives the interpolated parameter values for a, b, m, and C in 2.6,

In [10], Birnir and Chen found $l^\star$ was a constant. However, it became clear that when we include the Reynolds corrections and compensate by C_2 instead of C_1, $l^\star$ is not a constant but experiences an initial deviation before converging to a constant as $p \to \infty$. This can be seen in figure $A.60$. Note that $A.60$ is a plot of the $l^\star$ values that give exact agreement between the left

and right hand sides of equation 4.7. Hence, we see that $l^\star$ is a function depending upon p, but it appears to be independent of the Reynolds number.

Chapter 5

Conclusion

We started by following Kolmogorov's method as described in Chapter 2, and formulated in Landau and Lifschitz [3], to close the Navier Stokes equations to describe fully developed turbulence. We did this by introducing a stochastic forcing term to account for the small scales, see [1]. Having closed the model, we then compute a sine series representation for the structure functions of turbulence, with Reynolds number corrections. These formulas were then fitted to data generated from the Variable Density Turbulence Tunnel at the Max Planck Institute for Dynamics and Self-Organization. The fits proved to be very good and yielded valuable insights into the smoothness of the fluid velocity.

For the lower Reynolds number flows, we see convergence of the sine series for the second, third, and fourth structure functions. However, the sixth and eighth structure functions for these Reynolds numbers begin to show sign of divergence. For higher Reynolds number, this divergence becomes more pronounced, as the fourth structure function begins to diverge and the third one begins to show signs of spatial roughness (divergence), as well. This agrees with our theory and may be indicative of an increasing influence of intermittency as the Reynolds number increases.

We compared fits to the formulas for the structure functions with a correction, to account

for the Reynolds number, to fits without that correction. We see that the Reynolds correction formulas generate better fits as the Reynolds number decreases for lower structure functions but have little impact on the fits for the higher structure functions. Again, this agrees with theory on the smoothness of the fluid velocity.

The fits simplify the stochastic closure theory (SCT) for the Navier-Stokes equation. We obtain a SCT theory (3.2) with only three parameters, one corresponding to the variance in the functional Central Limit theorem part of the noise, a second one giving the rate in the Large Deviation part of the noise and finally an exponent that gives the spatial smoothness of the noise (decay in Fourier space). These three parameters depend on the Taylor-Reynolds number but are independent of the order of the structure functions.

Finally, we compared the SCT with data generated in the flow physics facility (FPF) at the University of New Hampshire. This was done to examine the relationship between the Townsend-Perry constants and the SCT. We impose a similarity hypothesis to relate the ratio of the constants to the ratio of the coefficients of the SCT. The full derivation proved problematic due to the compensation by C_1 factor. Thus, we refined the theory and attempt to compensate by $C_2^{\frac{1}{2}}$. We then see good agreement between the data and the SCT.

Several additional questions still remain. Earlier in this dissertation, we mentioned the probability distributions (PDF) of the structure functions. We know that the PDF are generalized hyperbolic distributions but it remains an open question as to the effect of the Reynolds number on these distributions. Additionally, the formulation of the SCT is based on Eulerian turbulence. For Lagrangian turbulence, no such equivalent formulation exists and could be developed.

Appendix A

Appendix

A.1 Figures

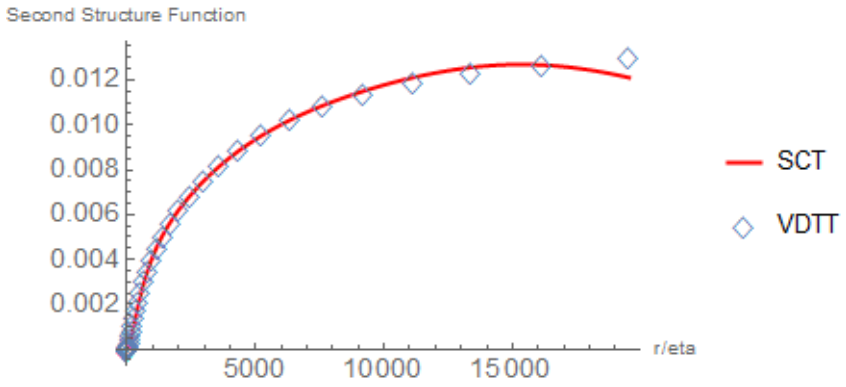

Figure A.1: Second Structure Function, Normal Scale. The blue diamonds correspond to the data from the VDTT whereas the red line is the fitted SCT. Taylor Reynolds number 110

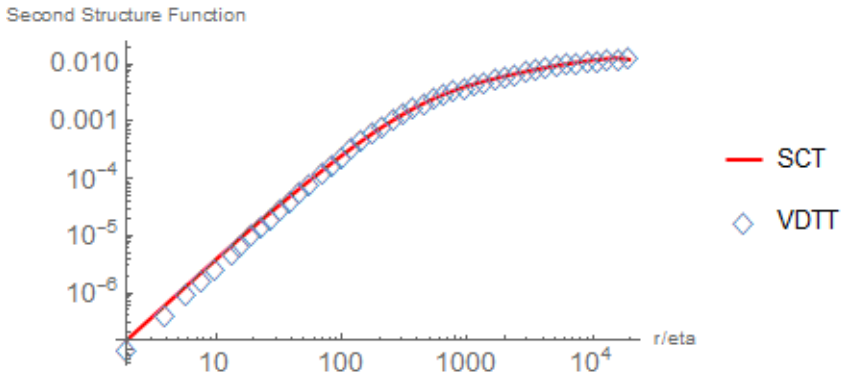

Figure A.2: Second Structure Function. The blue diamonds correspond to the data from the VDTT whereas the red line is the fitted SCT. Taylor Reynolds number 110

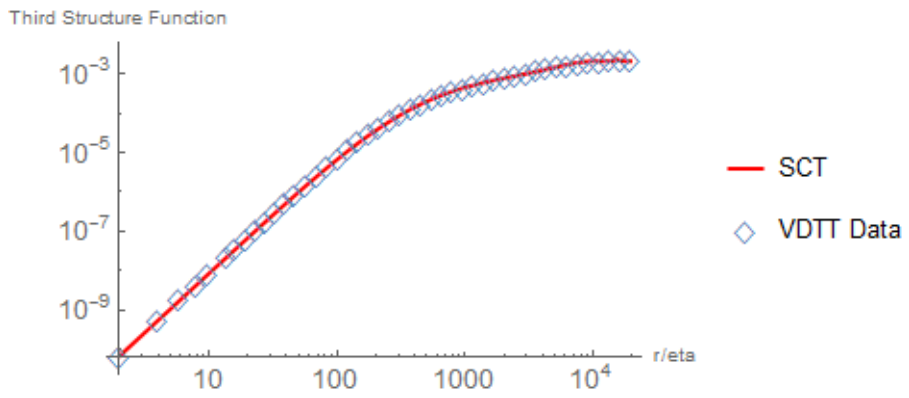

Figure A.3: Third Structure Function. The blue diamonds correspond to the data from the VDTT whereas the red line is the fitted SCT. Taylor Reynolds number 110

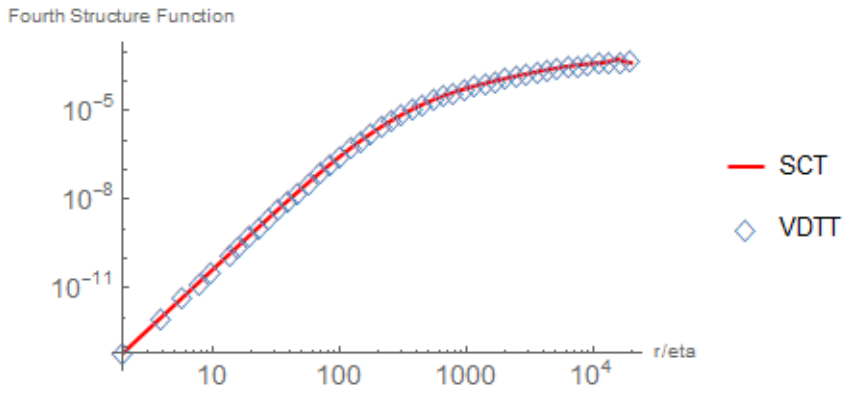

Figure A.4: Fourth StructureFunction. The blue diamonds correspond to the data from the VDTT whereas the red line is the fitted SCT. Taylor Reynolds number 110

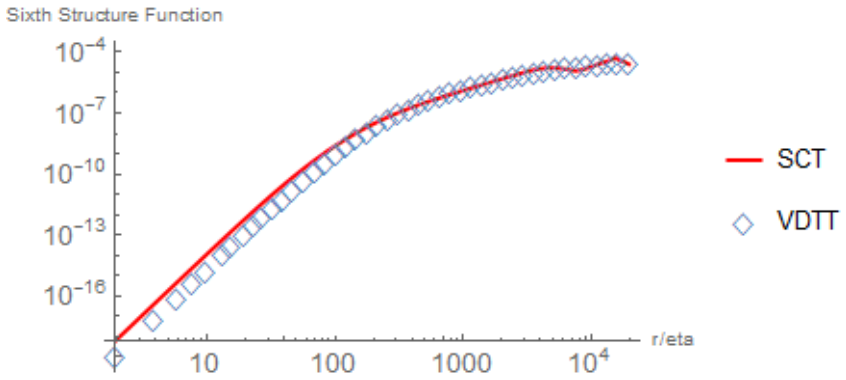

Figure A.5: Sixth Structure Function. The blue diamonds correspond to the data from the VDTT whereas the red line is the fitted SCT. Taylor Reynolds number 110

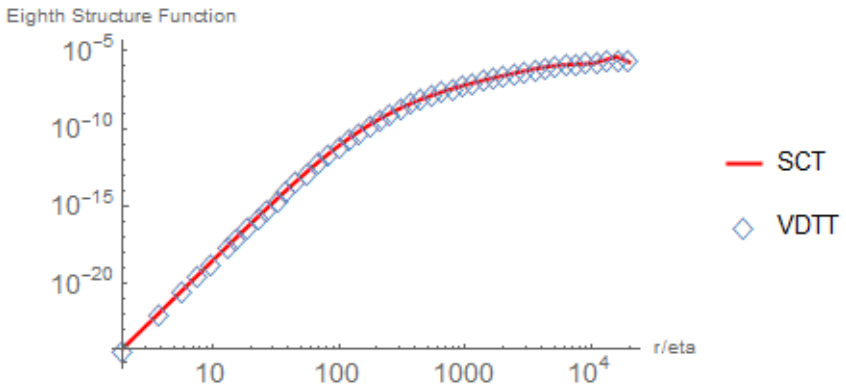

Figure A.6: Eighth Structure Function. The blue diamonds correspond to the data from the VDTT whereas the red line is the fitted SCT. Taylor Reynolds number 110

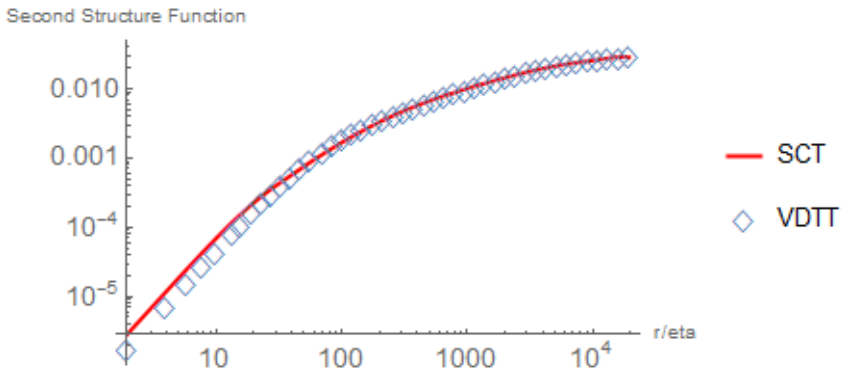

Figure A.7: Second Structure Function. The blue diamonds correspond to the data from the VDTT whereas the red line is the fitted SCT. Taylor Reynolds number 264

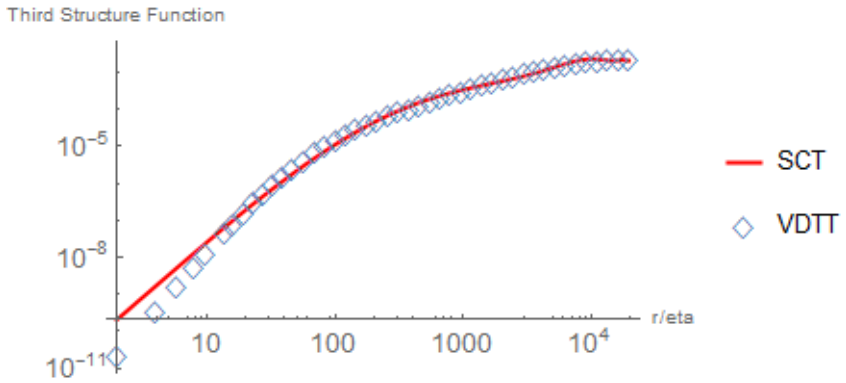

Figure A.8: Third Structure Function. The blue diamonds correspond to the data from the VDTT whereas the red line is the fitted SCT. Taylor Reynolds number 264

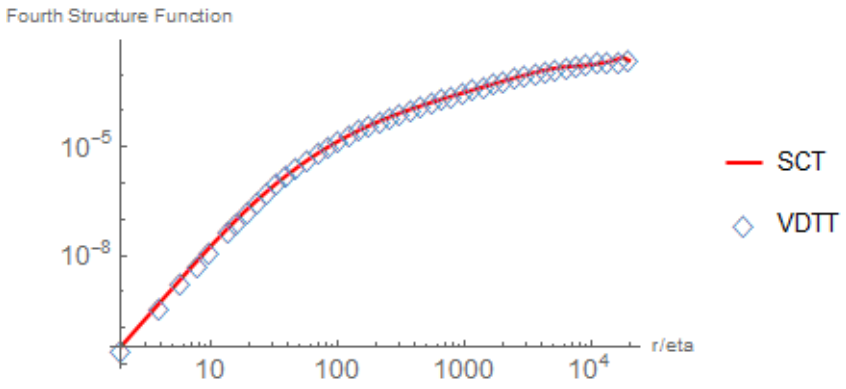

Figure A.9: Fourth StructureFunction. The blue diamonds correspond to the data from the VDTT whereas the red line is the fitted SCT. Taylor Reynolds number 264

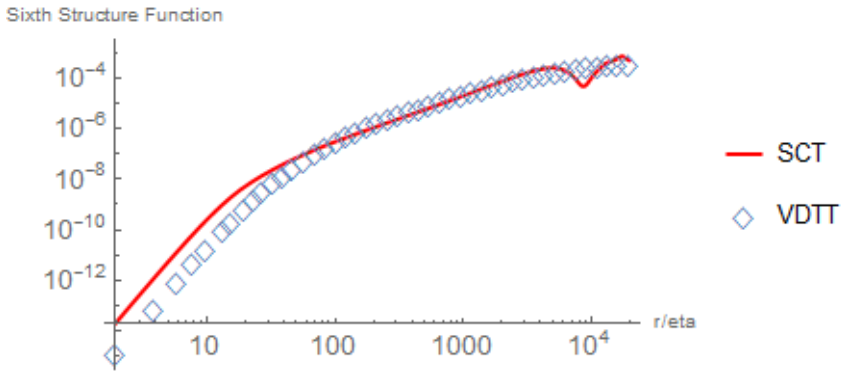

Figure A.10: Sixth Structure Function. The blue diamonds correspond to the data from the VDTT whereas the red line is the fitted SCT. Taylor Reynolds number 264

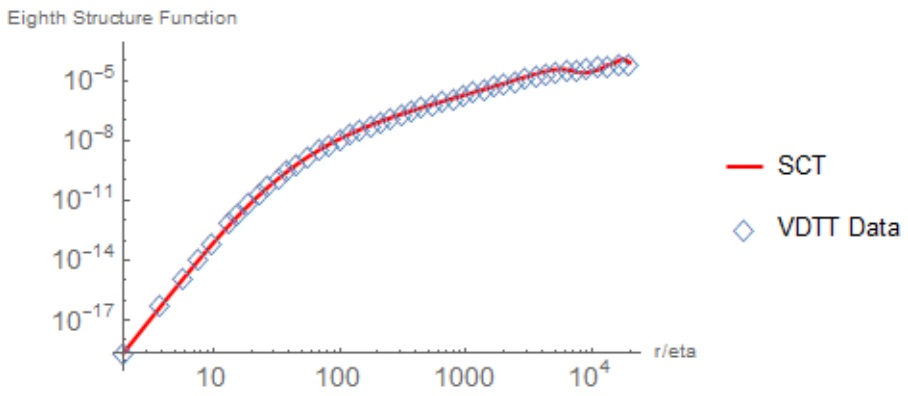

Figure A.11: Eighth Structure Function. The blue diamonds correspond to the data from the VDTT whereas the red line is the fitted SCT. Taylor Reynolds number 264

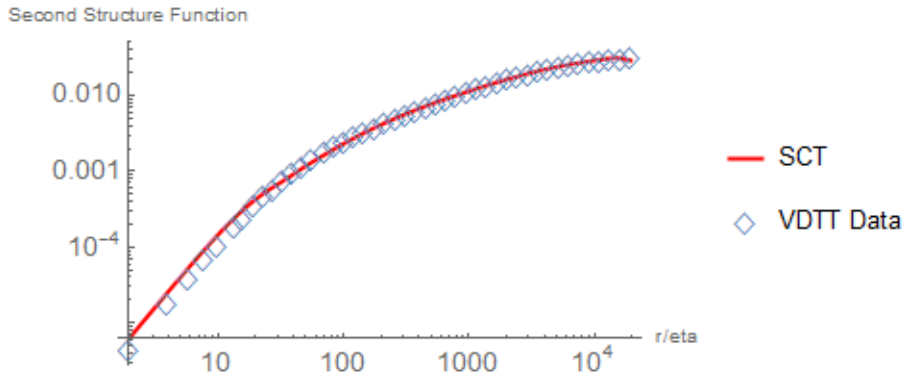

Figure A.12: Second Structure Function. The blue diamonds correspond to the data from the VDTT whereas the red line is the fitted SCT. Taylor Reynolds number 508

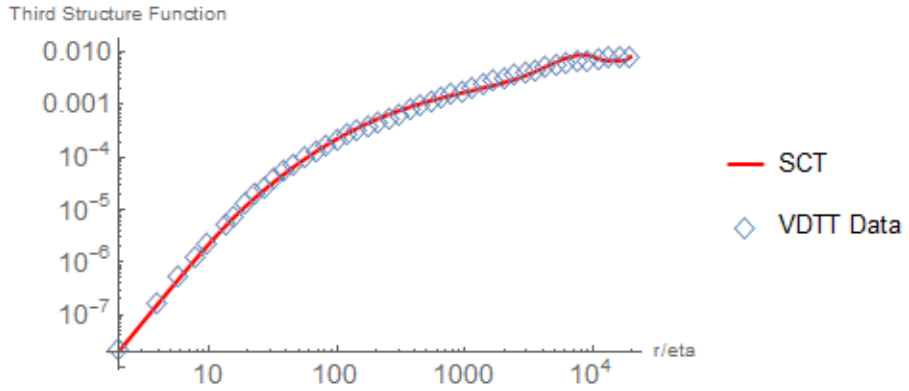

Figure A.13: Third Structure Function. The blue diamonds correspond to the data from the VDTT whereas the red line is the fitted SCT. Taylor Reynolds number 508

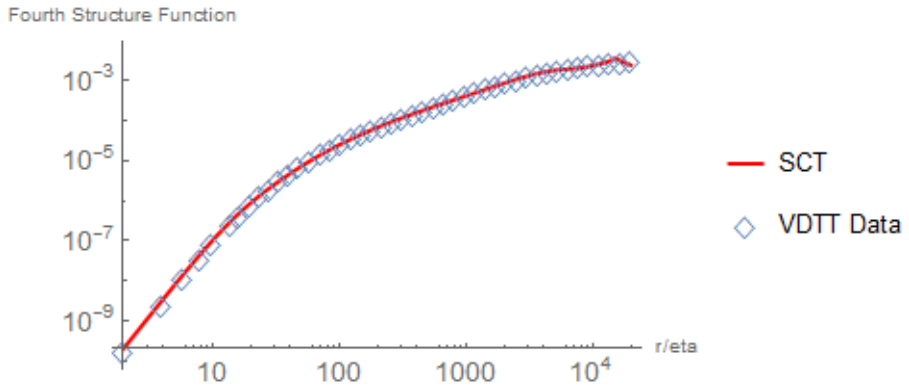

Figure A.14: Fourth StructureFunction. The blue diamonds correspond to the data from the VDTT whereas the red line is the fitted SCT. Taylor Reynolds number 508

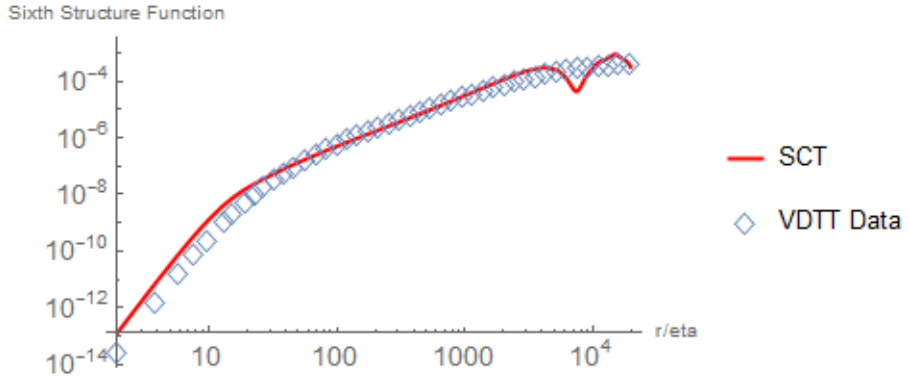

Figure A.15: Sixth Structure Function. The blue diamonds correspond to the data from the VDTT whereas the red line is the fitted SCT. Taylor Reynolds number 508

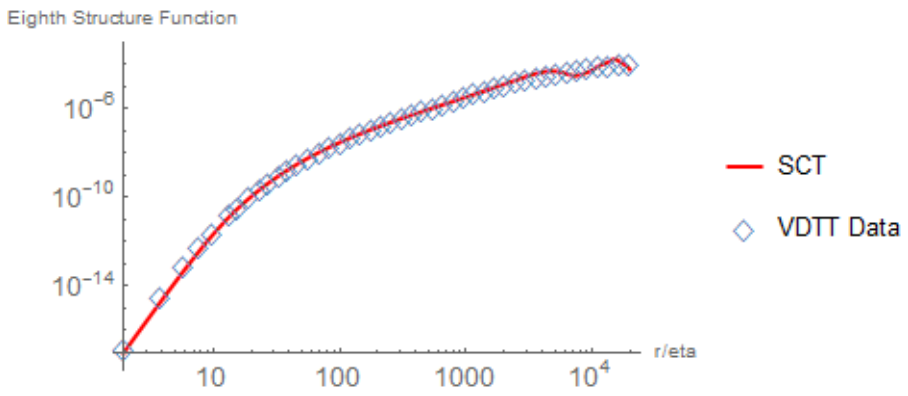

Figure A.16: Eighth Structure Function. The blue diamonds correspond to the data from the VDTT whereas the red line is the fitted SCT. Taylor Reynolds number 508

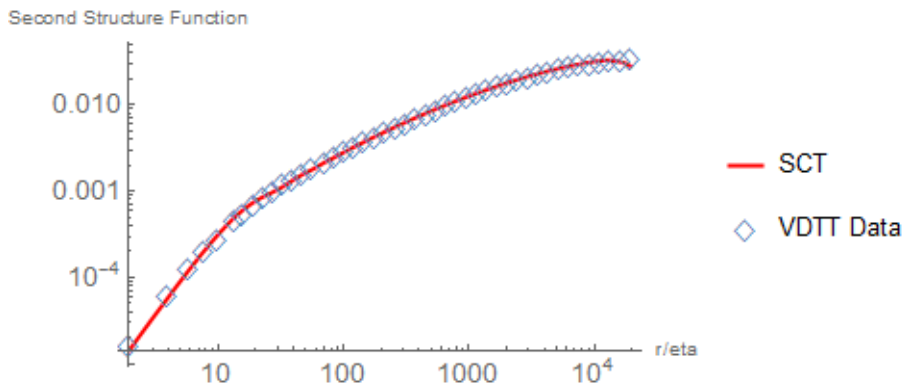

Figure A.17: Second Structure Function. The blue diamonds correspond to the data from the VDTT whereas the red line is the fitted SCT. Taylor Reynolds number 1000

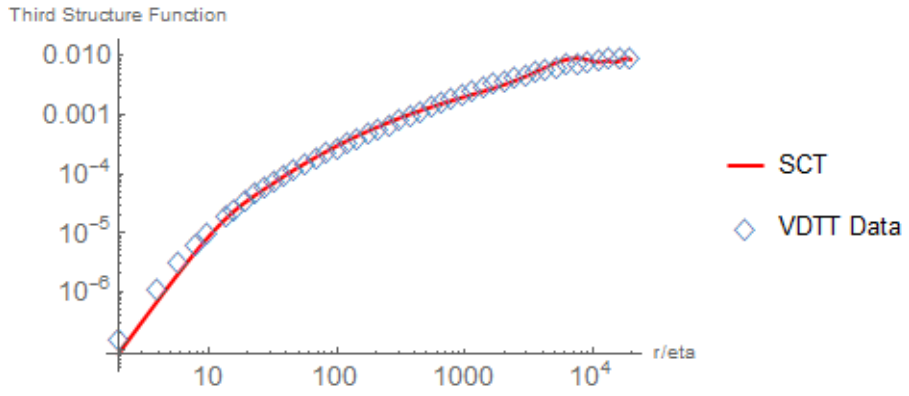

Figure A.18: Third Structure Function. The blue diamonds correspond to the data from the VDTT whereas the red line is the fitted SCT. Taylor Reynolds number 1000

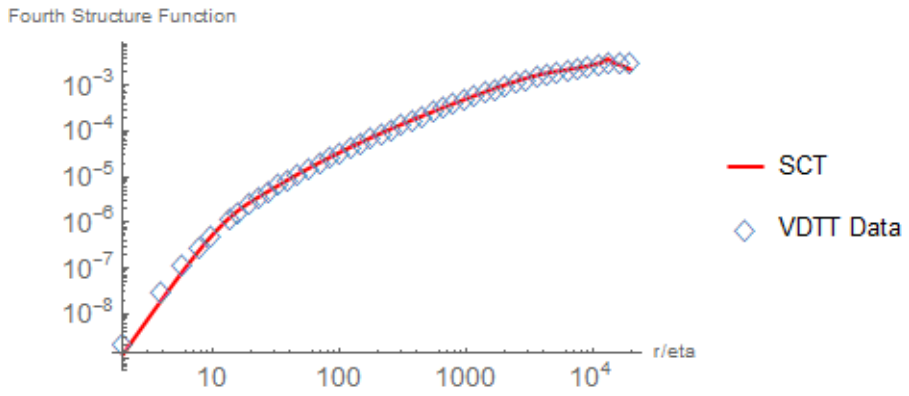

Figure A.19: Fourth StructureFunction. The blue diamonds correspond to the data from the VDTT whereas the red line is the fitted SCT. Taylor Reynolds number 1000

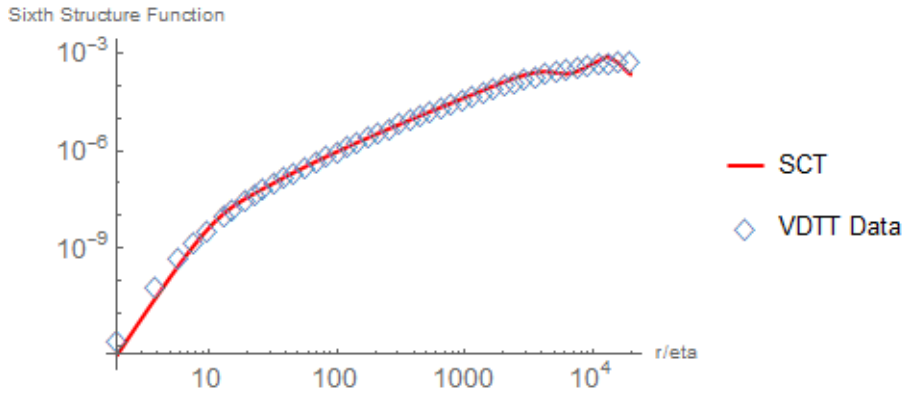

Figure A.20: Sixth Structure Function. The blue diamonds correspond to the data from the VDTT whereas the red line is the fitted SCT. Taylor Reynolds number 1000

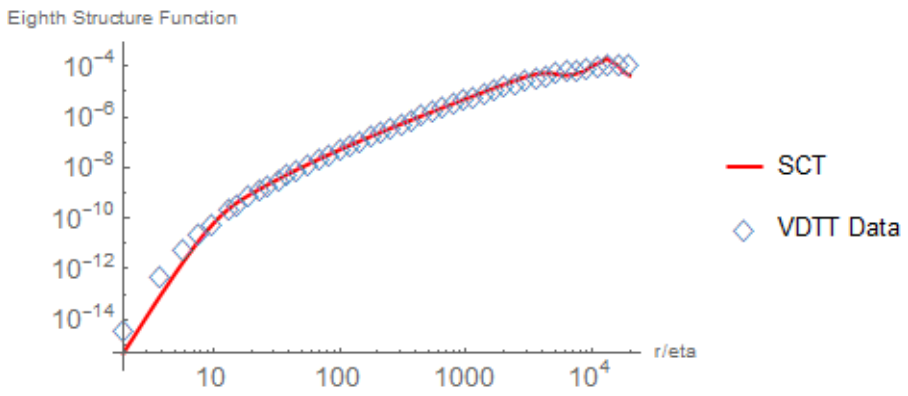

Figure A.21: Eighth Structure Function. The blue diamonds correspond to the data from the VDTT whereas the red line is the fitted SCT. Taylor Reynolds number 1000

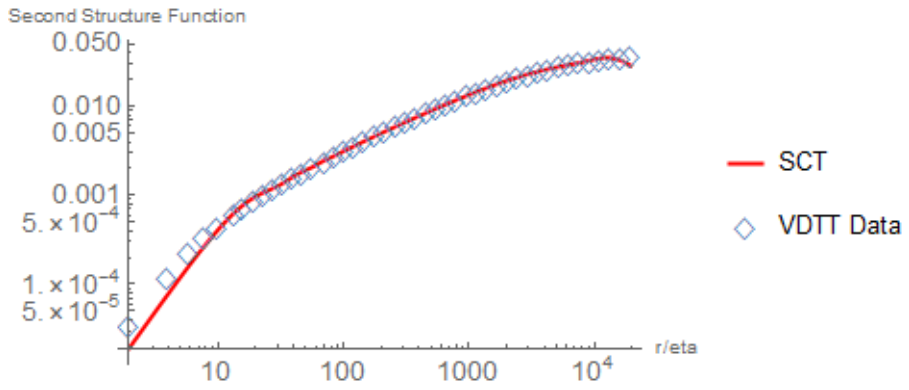

Figure A.22: Second Structure Function. The blue diamonds correspond to the data from the VDTT whereas the red line is the fitted SCT. Taylor Reynolds number 1450

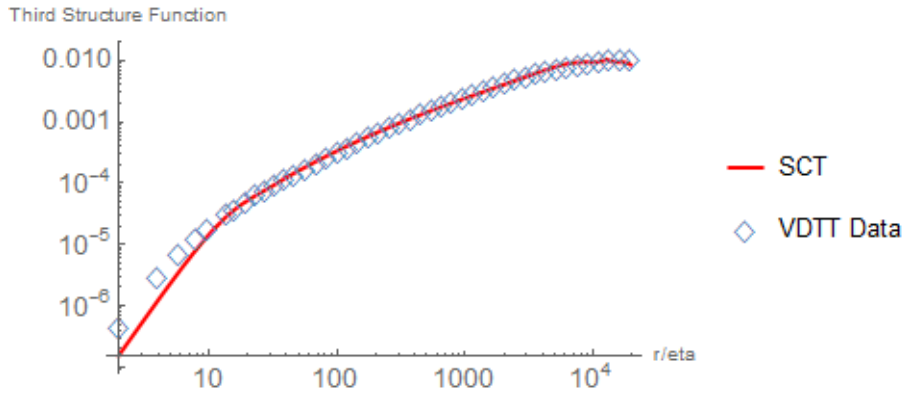

Figure A.23: Third Structure Function. The blue diamonds correspond to the data from the VDTT whereas the red line is the fitted SCT. Taylor Reynolds number 1450

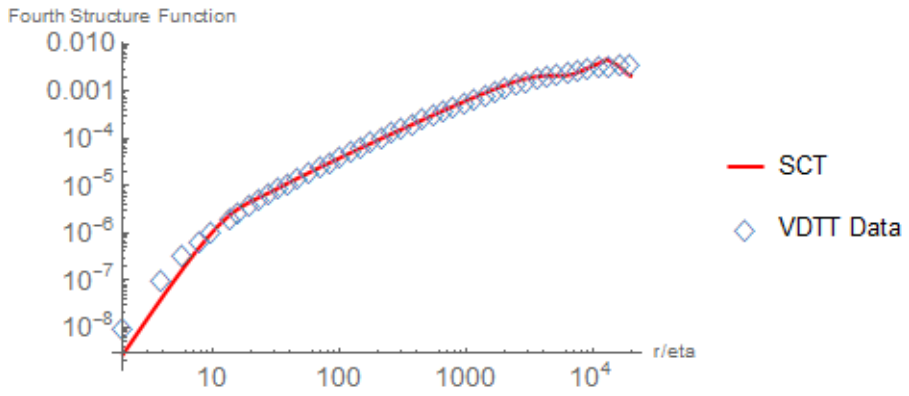

Figure A.24: Fourth StructureFunction. The blue diamonds correspond to the data from the VDTT whereas the red line is the fitted SCT. Taylor Reynolds number 1450

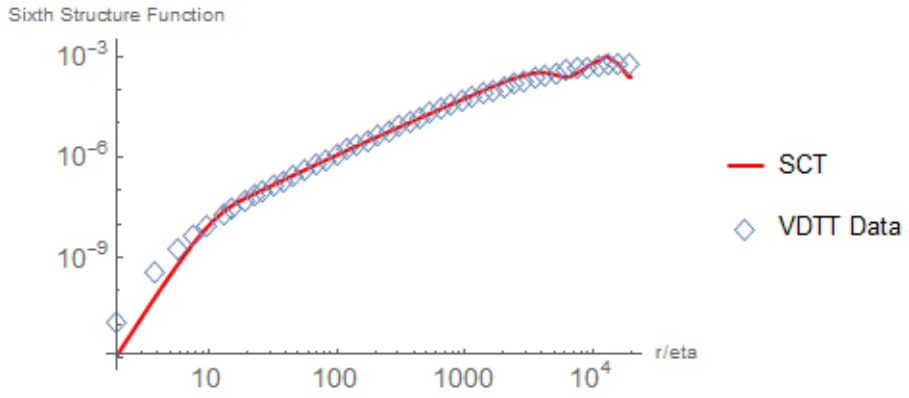

Figure A.25: Sixth Structure Function. The blue diamonds correspond to the data from the VDTT whereas the red line is the fitted SCT. Taylor Reynolds number 1450

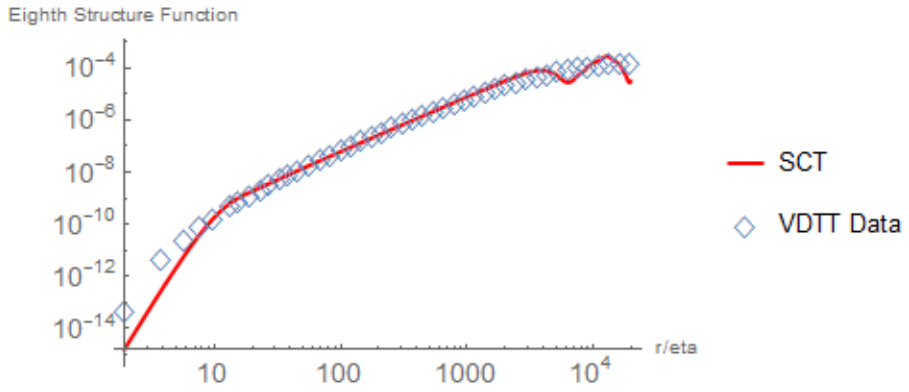

Figure A.26: Eighth Structure Function. The blue diamonds correspond to the data from the VDTT whereas the red line is the fitted SCT. Taylor Reynolds number 1450

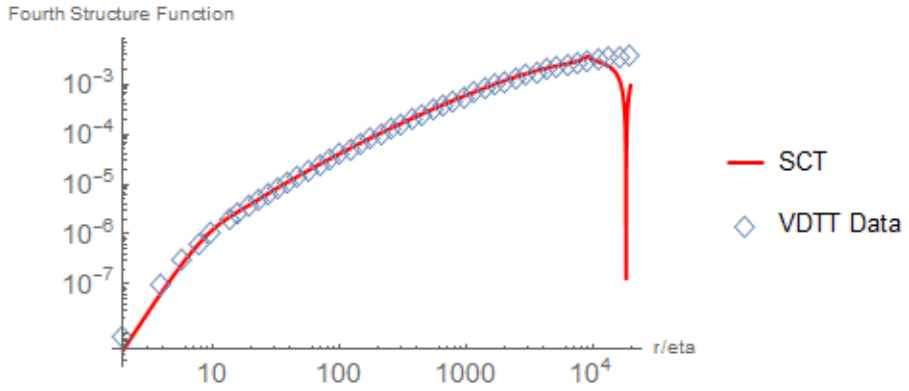

Figure A.27: Fourth Structure Function at $D = 0.920864$ for Reynolds number 1450

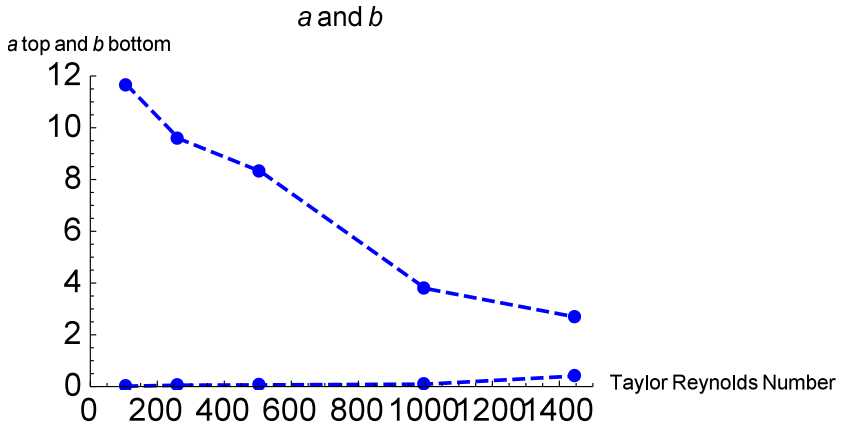

Figure A.28: The coefficients a and b.

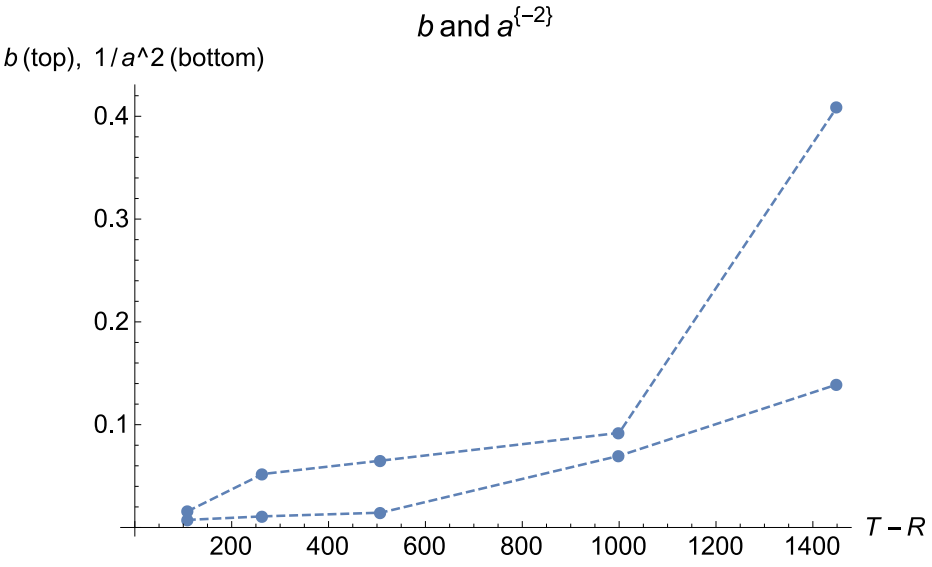

Figure A.29: The coefficients b and $\frac{1}{a^2}$.

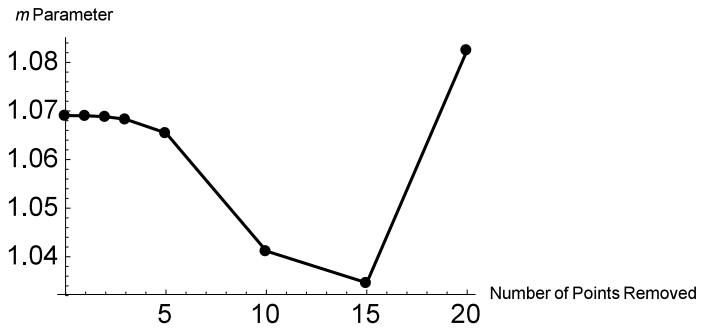

Figure A.30: Second Structure Function. Robustness test for Reynolds number 508. Note the scales on the y-axis

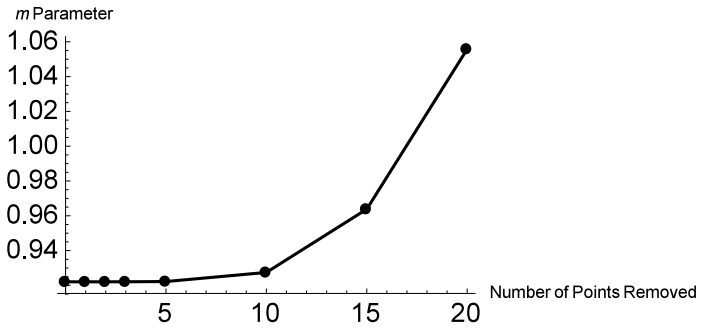

Figure A.31: Third Structure Function. Robustness test for Reynolds number 508. Note the scales on the y-axis

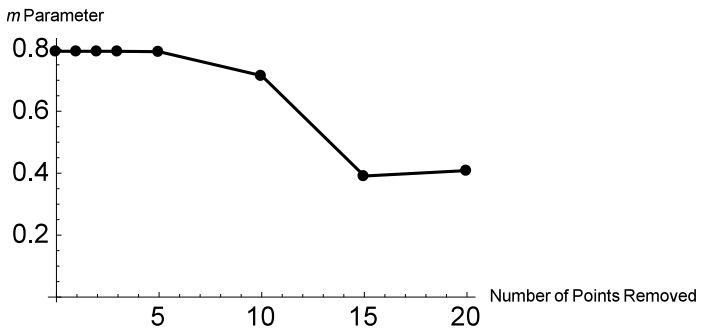

Figure A.32: Fourth StructureFunction. Robustness test for Reynolds number 508. Note the scales on the y-axis

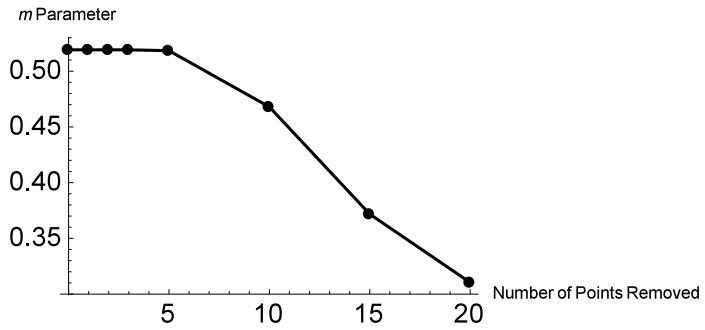

Figure A.33: Sixth Structure Function. Robustness test for Reynolds number 508. Note the scales on the y-axis

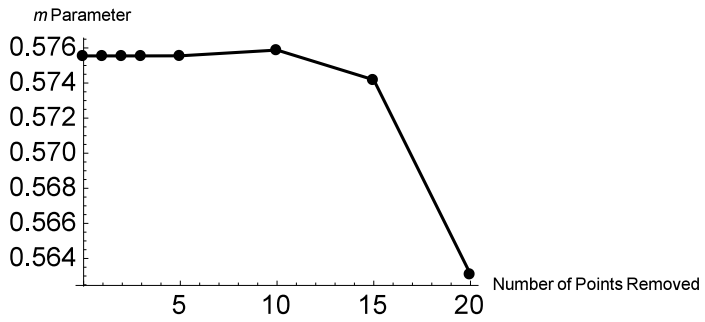

Figure A.34: Eighth Structure Function. Robustness test for Reynolds number 508. Note the scales on the y-axis

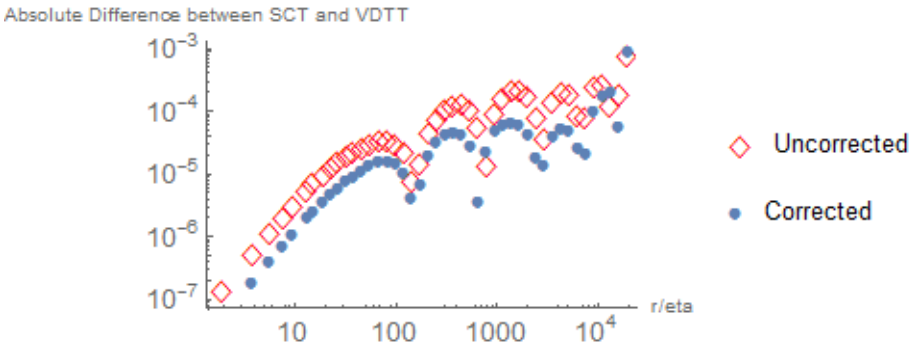

Figure A.35: Error for Taylor Reynolds Number 110. Note that the plots are made on a log-log scale. The blue dots are fits to the structure function formula featuring the Reynolds correction whereas the red diamonds are fits to the structure function formula without the Reynolds number correction. Second Structure Function Error.

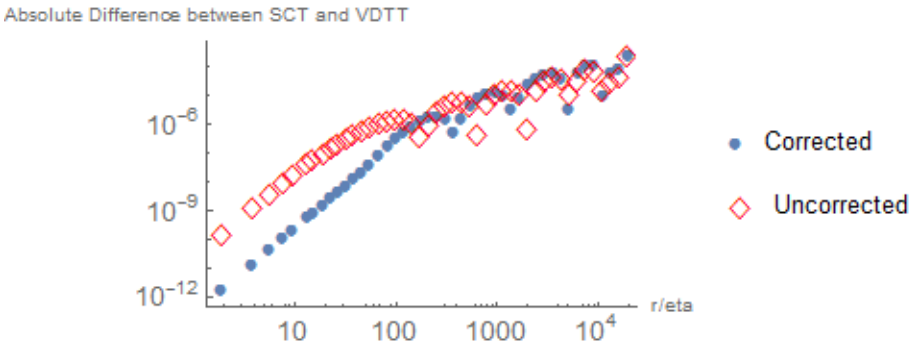

Figure A.36: Error for Taylor Reynolds Number 110. Note that the plots are made on a log-log scale. The blue dots are fits to the structure function formula featuring the Reynolds correction whereas the red diamonds are fits to the structure function formula without the Reynolds number correction. Third Structure Function Error.

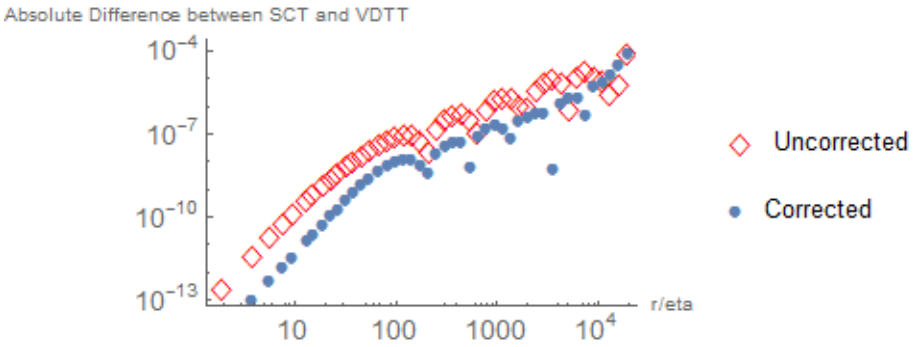

Figure A.37: Error for Taylor Reynolds Number 110. Note that the plots are made on a log-log scale. The blue dots are fits to the structure function formula featuring the Reynolds correction whereas the red diamonds are fits to the structure function formula without the Reynolds number correction. Fourth Structure Function Error.

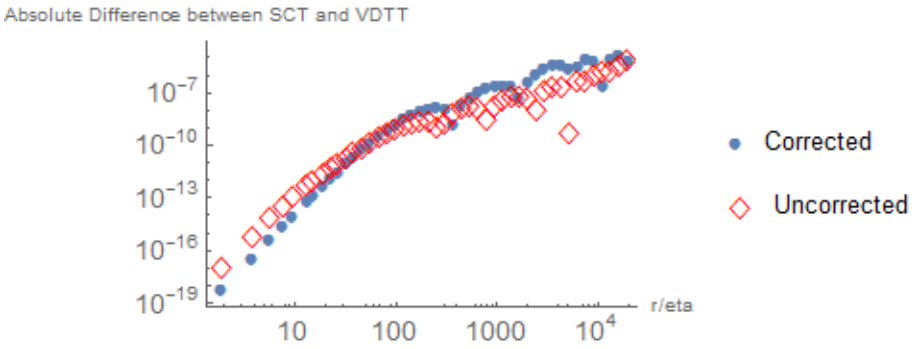

Figure A.38: Error for Taylor Reynolds Number 110. Note that the plots are made on a log-log scale. The blue dots are fits to the structure function formula featuring the Reynolds correction whereas the red diamonds are fits to the structure function formula without the Reynolds number correction. Sixth Structure Function Error.

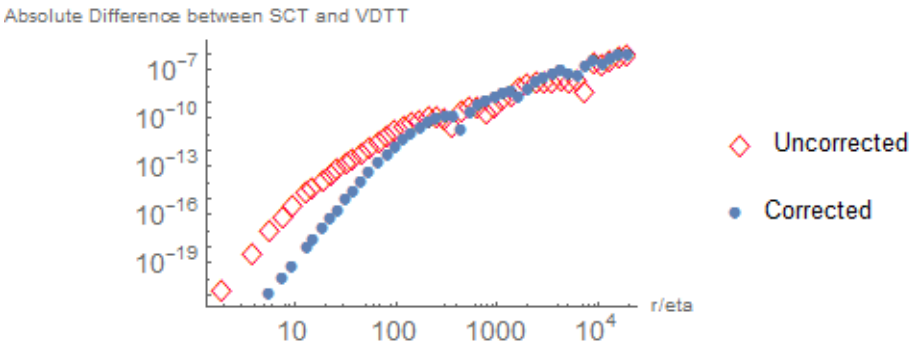

Figure A.39: Error for Taylor Reynolds Number 110. Note that the plots are made on a log-log scale. The blue dots are fits to the structure function formula featuring the Reynolds correction whereas the red diamonds are fits to the structure function formula without the Reynolds number correction. Eighth Structure Function Error.

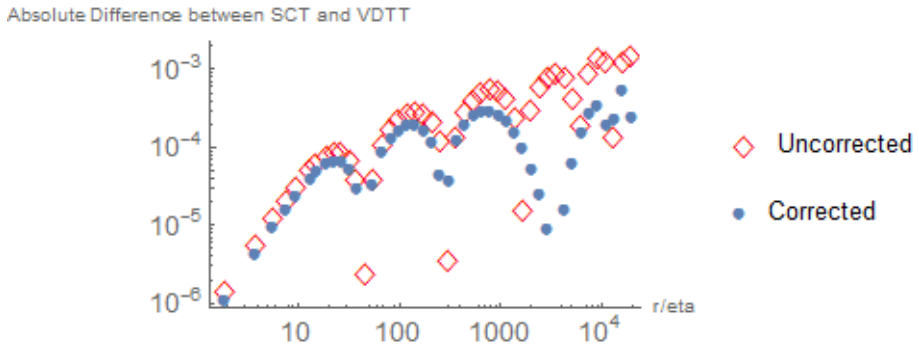

Figure A.40: Error for Taylor Reynolds Number 264. Note that the plots are made on a log-log scale. The blue dots are fits to the structure function formula featuring the Reynolds correction whereas the red diamonds are fits to the structure function formula without the Reynolds number correction. Second Structure Function Error

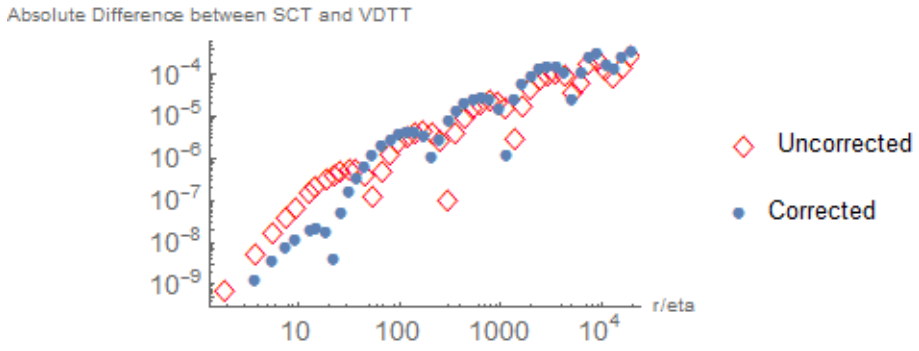

Figure A.41: Error for Taylor Reynolds Number 264. Note that the plots are made on a log-log scale. The blue dots are fits to the structure function formula featuring the Reynolds correction whereas the red diamonds are fits to the structure function formula without the Reynolds number correction. Third Structure Function Error

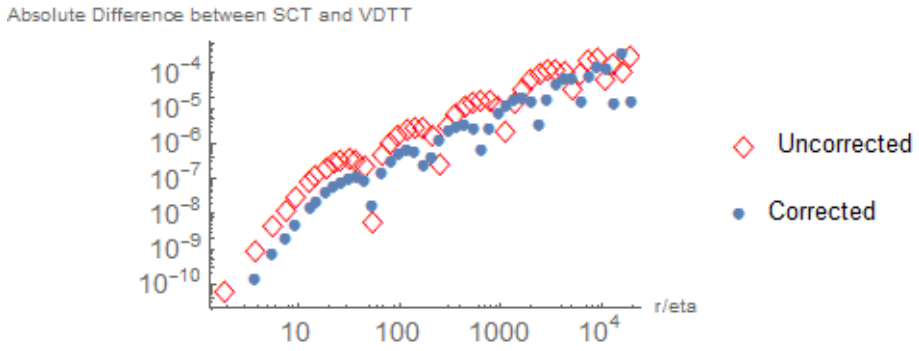

Figure A.42: Error for Taylor Reynolds Number 264. Note that the plots are made on a log-log scale. The blue dots are fits to the structure function formula featuring the Reynolds correction whereas the red diamonds are fits to the structure function formula without the Reynolds number correction. Fourth Structure Function Error

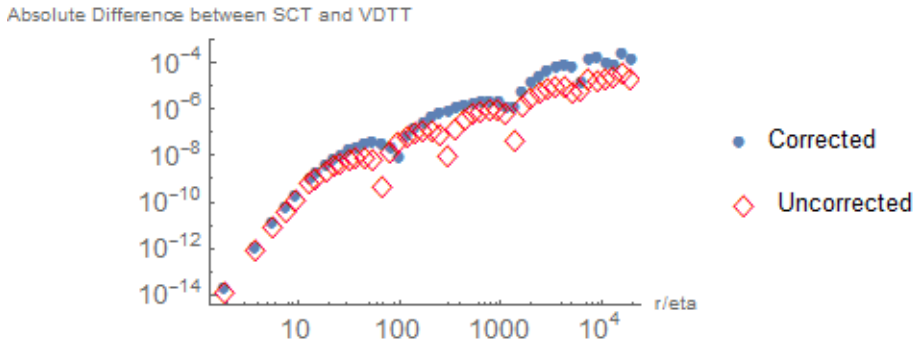

Figure A.43: Error for Taylor Reynolds Number 264. Note that the plots are made on a log-log scale. The blue dots are fits to the structure function formula featuring the Reynolds correction whereas the red diamonds are fits to the structure function formula without the Reynolds number correction. Sixth Structure Function Error

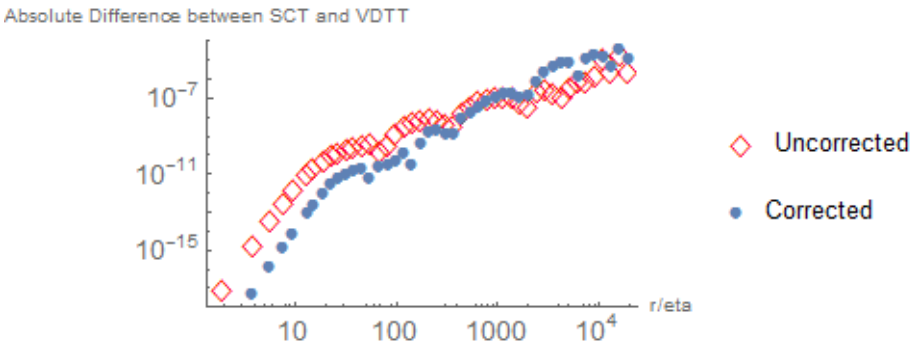

Figure A.44: Error for Taylor Reynolds Number 264. Note that the plots are made on a log-log scale. The blue dots are fits to the structure function formula featuring the Reynolds correction whereas the red diamonds are fits to the structure function formula without the Reynolds number correction. Eighth Structure Function Error

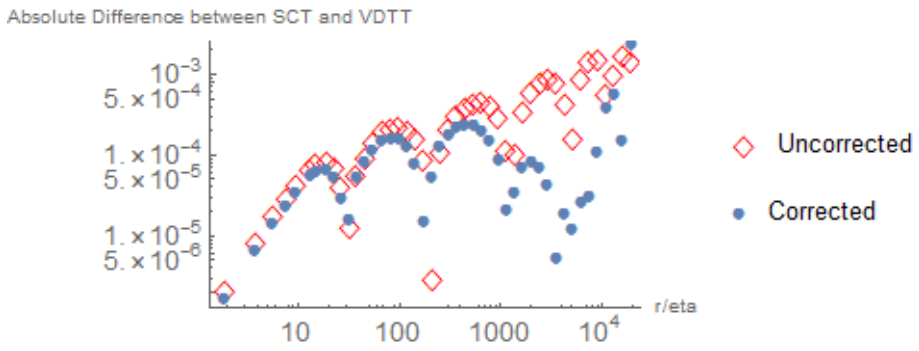

Figure A.45: Error for Taylor Reynolds Number 508. Note that the plots are made on a log-log scale. The blue dots are fits to the structure function formula featuring the Reynolds correction whereas the red diamonds are fits to the structure function formula without the Reynolds number correction. Second Structure Function Error

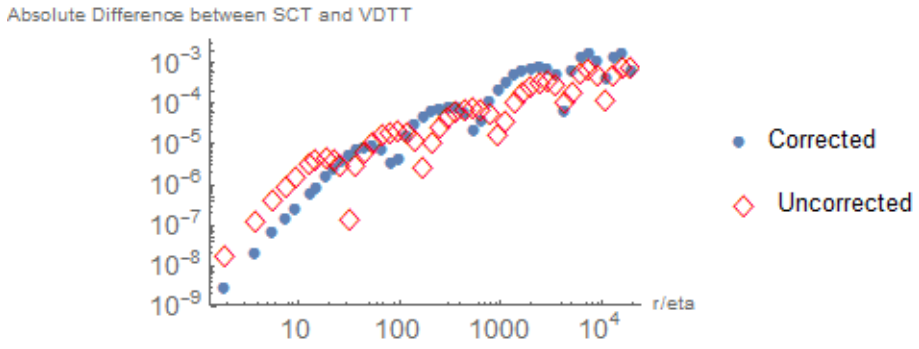

Figure A.46: Error for Taylor Reynolds Number 508. Note that the plots are made on a log-log scale. The blue dots are fits to the structure function formula featuring the Reynolds correction whereas the red diamonds are fits to the structure function formula without the Reynolds number correction. Third Structure Function Error

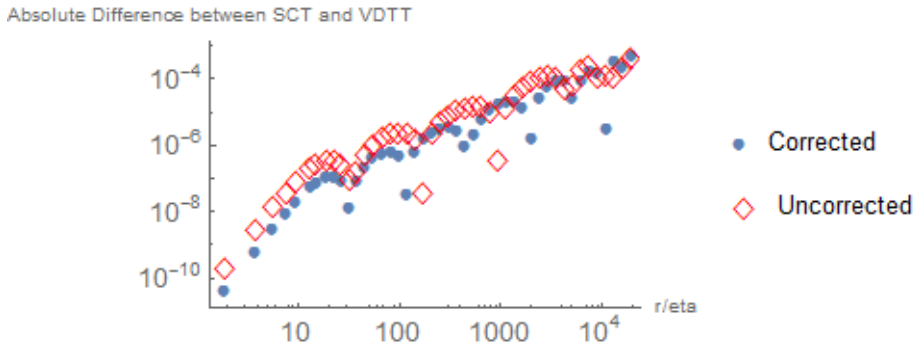

Figure A.47: Error for Taylor Reynolds Number 508. Note that the plots are made on a log-log scale. The blue dots are fits to the structure function formula featuring the Reynolds correction whereas the red diamonds are fits to the structure function formula without the Reynolds number correction. Fourth Structure Function Error

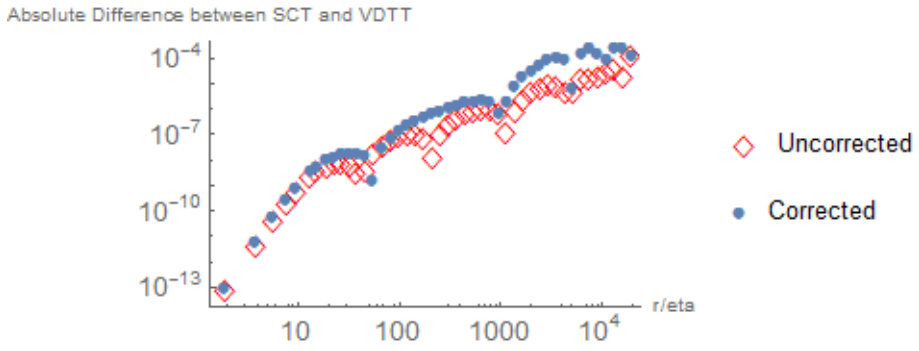

Figure A.48: Error for Taylor Reynolds Number 508. Note that the plots are made on a log-log scale. The blue dots are fits to the structure function formula featuring the Reynolds correction whereas the red diamonds are fits to the structure function formula without the Reynolds number correction. Sixth Structure Function Error

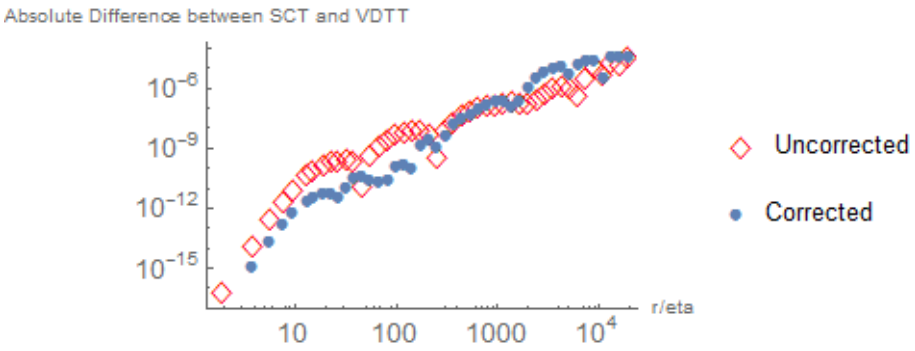

Figure A.49: Error for Taylor Reynolds Number 508. Note that the plots are made on a log-log scale. The blue dots are fits to the structure function formula featuring the Reynolds correction whereas the red diamonds are fits to the structure function formula without the Reynolds number correction. Eighth Structure Function Error

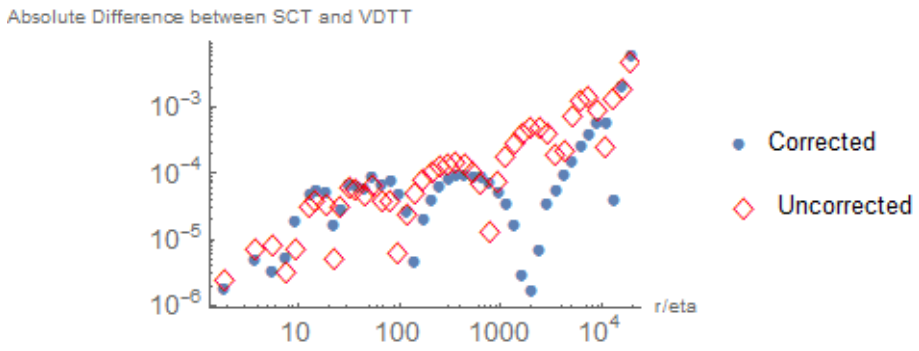

Figure A.50: Error for Taylor Reynolds Number 1000. Note that the plots are made on a log-log scale. The blue dots are fits to the structure function formula featuring the Reynolds correction whereas the red diamonds are fits to the structure function formula without the Reynolds number correction. Second Structure Function Error

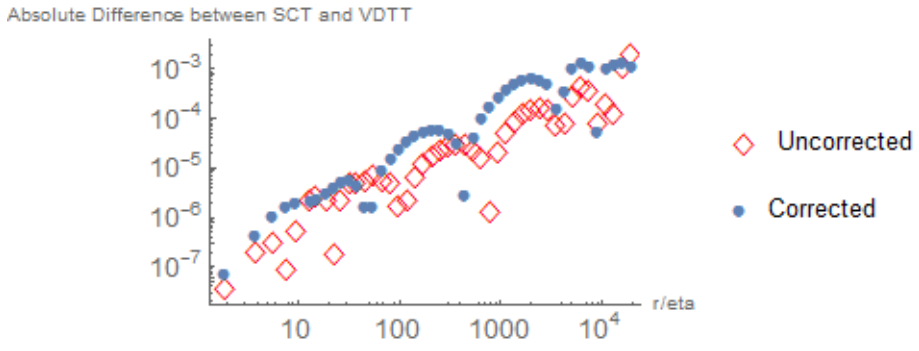

Figure A.51: Error for Taylor Reynolds Number 1000. Note that the plots are made on a log-log scale. The blue dots are fits to the structure function formula featuring the Reynolds correction whereas the red diamonds are fits to the structure function formula without the Reynolds number correction. Third Structure Function Error

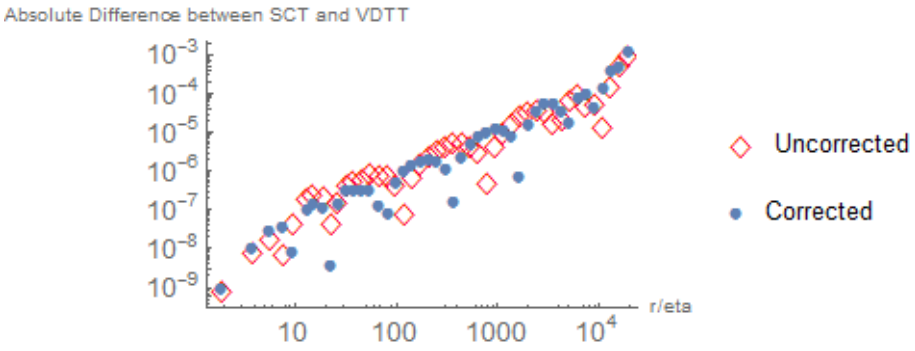

Figure A.52: Error for Taylor Reynolds Number 1000. Note that the plots are made on a log-log scale. The blue dots are fits to the structure function formula featuring the Reynolds correction whereas the red diamonds are fits to the structure function formula without the Reynolds number correction. Fourth Structure Function Error

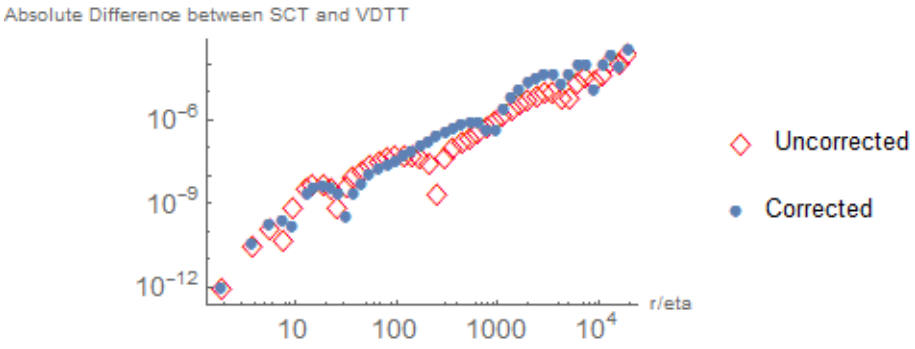

Figure A.53: Error for Taylor Reynolds Number 1000. Note that the plots are made on a log-log scale. The blue dots are fits to the structure function formula featuring the Reynolds correction whereas the red diamonds are fits to the structure function formula without the Reynolds number correction. Sixth Structure Function Error

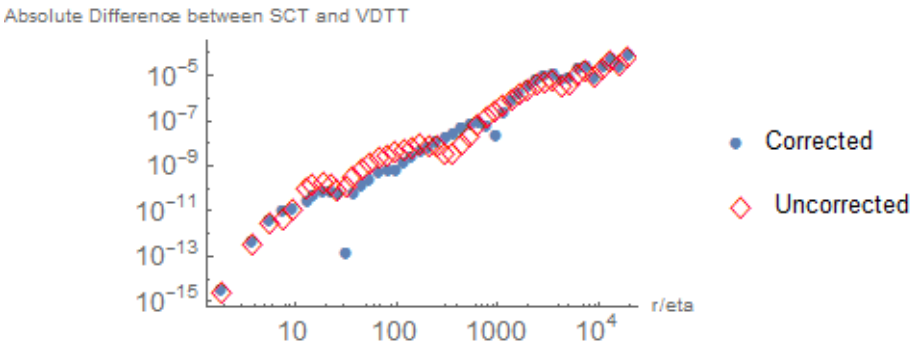

Figure A.54: Error for Taylor Reynolds Number 1000. Note that the plots are made on a log-log scale. The blue dots are fits to the structure function formula featuring the Reynolds correction whereas the red diamonds are fits to the structure function formula without the Reynolds number correction. Eighth Structure Function Error

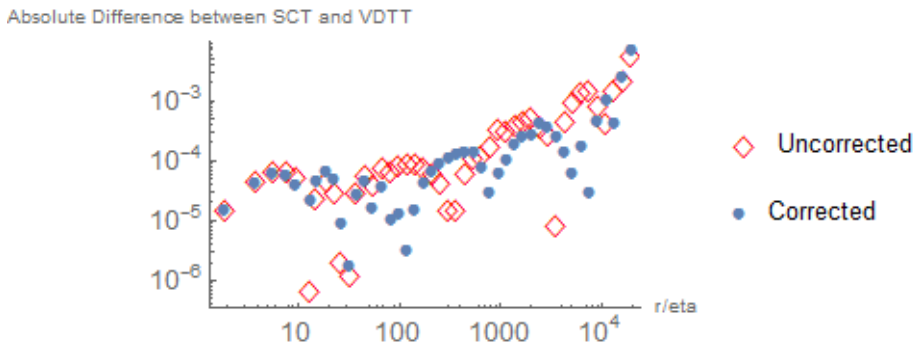

Figure A.55: Error for Taylor Reynolds Number 1450. Note that the plots are made on a log-log scale. The blue dots are fits to the structure function formula featuring the Reynolds correction whereas the red diamonds are fits to the structure function formula without the Reynolds number correction. Second Structure Function Error

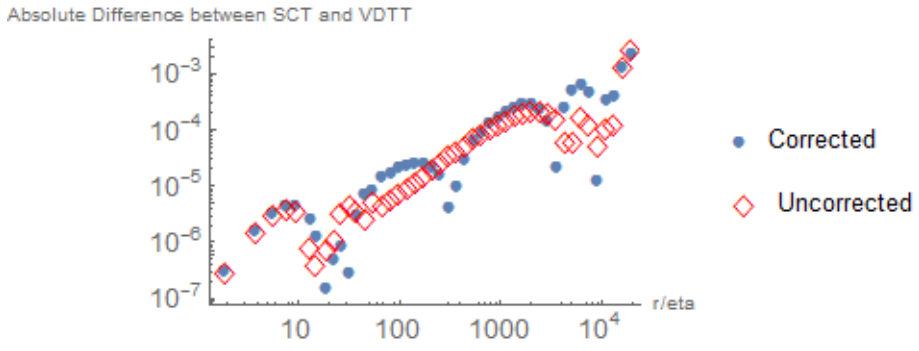

Figure A.56: Error for Taylor Reynolds Number 1450. Note that the plots are made on a log-log scale. The blue dots are fits to the structure function formula featuring the Reynolds correction whereas the red diamonds are fits to the structure function formula without the Reynolds number correction. Third Structure Function Error

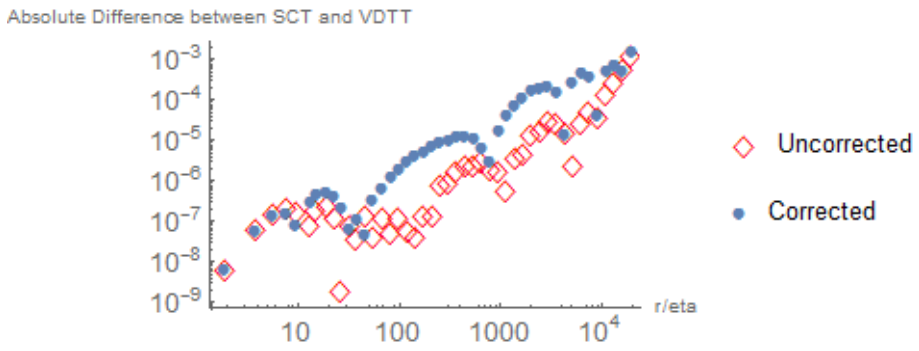

Figure A.57: Error for Taylor Reynolds Number 1450. Note that the plots are made on a log-log scale. The blue dots are fits to the structure function formula featuring the Reynolds correction whereas the red diamonds are fits to the structure function formula without the Reynolds number correction. Fourth Structure Function Error

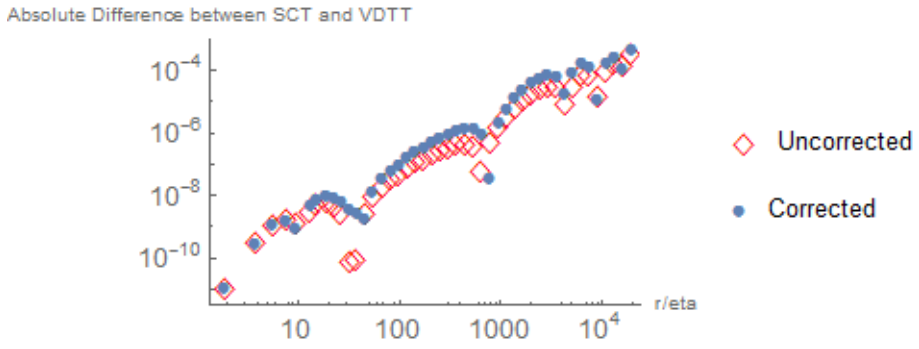

Figure A.58: Error for Taylor Reynolds Number 1450. Note that the plots are made on a log-log scale. The blue dots are fits to the structure function formula featuring the Reynolds correction whereas the red diamonds are fits to the structure function formula without the Reynolds number correction. Sixth Structure Function Error

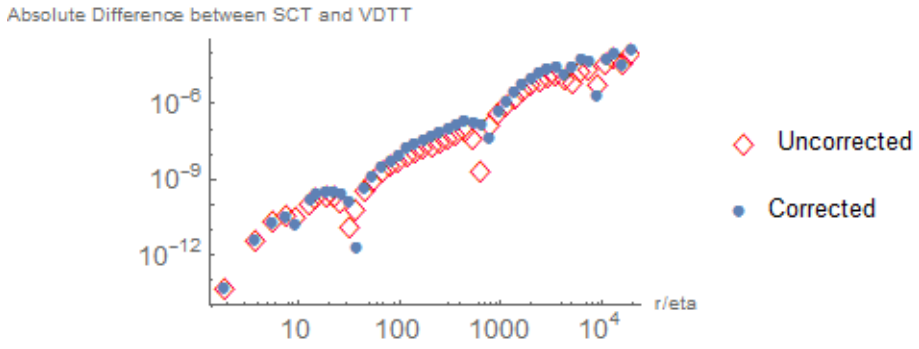

Figure A.59: Error for Taylor Reynolds Number 1450. Note that the plots are made on a log-log scale. The blue dots are fits to the structure function formula featuring the Reynolds correction whereas the red diamonds are fits to the structure function formula without the Reynolds number correction. Eighth Structure Function Error

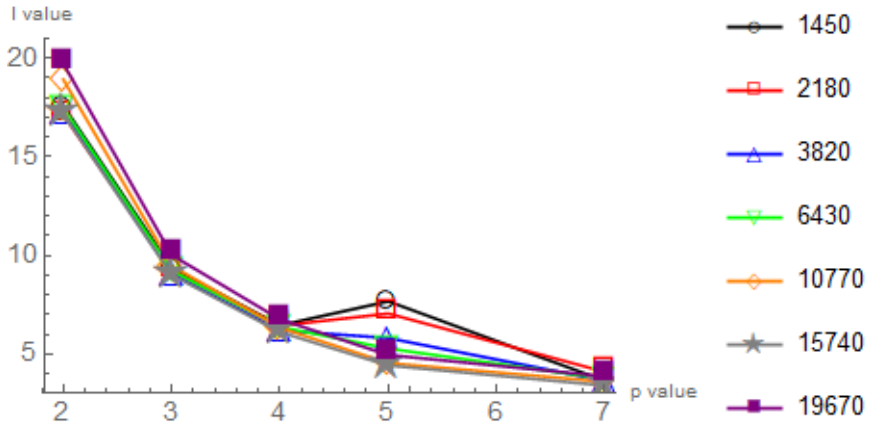

Figure A.60: The plot of $l^{\star}$ values that give exact agreement between the formula 4.7 and $\frac{\alpha_p}{\alpha_1}$.

Appendix B

Appendix

B.1 Mathematica Code for Wind Tunnel Data

```
(*Please note that fitting for the other Taylor Reynolds Number is similar*)

h[k_, r_, L_, nu_, a_, b_, m_, R_] :=
 (8 / L^3) * (Abs[Sin[Pi * k * r / (19540.3 (R))]])^3 * (((L / 2) *
       ((Sqrt[2 / Pi] * Abs[b] / (b^2 + k^m)))^2 * (Abs[(Sqrt[2 / Pi] * Abs[a] / (a + k^m))])) /
     (Abs[k] + (((8 * Pi^2 * nu) / L) * Abs[k]^(7 / 3)) + (((16 * Pi^4 * nu^2) / (L^2)) *
          Abs[k]^(11 / 3))) + ((Abs[(Sqrt[2 / Pi] * Abs[a] / (a^2 + k^m))])^3 /
      (Abs[k] + (((12 * Pi^2 * nu) / L) * Abs[k]^(7 / 3)) + (((48 * Pi^4 * nu^2) / (L^2)) *
          Abs[k]^(11 / 3)) + (((64 * Pi^6 * nu^3) / (L^3)) * Abs[k]^5))))
(*This is the formula for the third structure function*)

v3 =
  ReadList["C:\\Users\\John\\Desktop\\MPIDSReLambda110\\110AThirdStructureFunction.txt",
   "Number"];
(*Data for third structure function*)

x = ReadList["C:\\Users\\John\\Desktop\\MPIDSRELambda264\\RoverEta.txt", "Number"];
(*r/eta values*)

y3 = v3 / x;
(*Compensating by r^zeta_p yields better accuracy results for the fitting.  Thus,
we divide the third structure function data by r, as zeta_3=1*)

u3 = Transpose[{x, y3}];

q3 = Transpose[{x, v3}];

FindFit[u3, (A1 * Abs[Sin[Pi * r / (19540.3 (1.56917))]]^3 +
    A2 * Abs[Sin[Pi * r * 2 / (19540.3 (1.56917))]]^3 +
    Sum[h[k, r, L, .00001546, 11.6425, 0.0161237, m, 1.56917], {k, 3, 1000}]) / r,
 {L, {m, 1.3}, A1, A2}, r, MaxIterations → 10000]
(*Here we fit to the third structure function*)

{L → 1.4002225711926906`, m → 1.4079545829778202`,
 A1 → 0.0015364993030136285`, A2 → 0.000871958092157627`
```

```
Show[LogLogPlot[(0.0015365 * Abs[Sin[Pi * r / (19540.3 (1.56917))]]^3 +
     0.000871958 * Abs[Sin[Pi * r * 2 / (19540.3 (1.56917))]]^3 +
     Sum[h[k, r, 1.40022, .00001546, 11.6425, 0.0161237, 1.40795, 1.56917], {k, 3, 1000}]),
  {r, 1.95403, Max[q3]}, PlotRange → All, PlotStyle → {Red, Thick}, TicksStyle → Larger],
 ListLogLogPlot[q3, PlotRange → All, PlotMarkers → {◇, 20}]]
(*Here we plot the results of the third structure function fit against the data*)
```

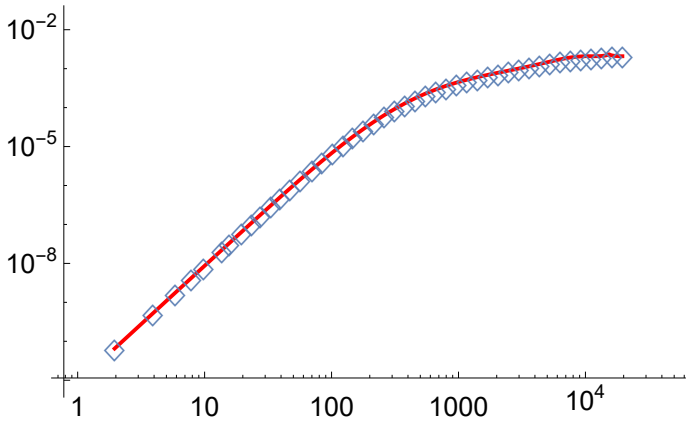


```
g[k_, r_, L_, nu_, a_, b_, m_, R_] :=
 (4 / L^2) * (((Abs[L] / 2) * ((Sqrt[2 / Pi] * Abs[b] / (b^2 + k^m)))) /
     (Abs[k]^((2 / 3) - (4 / 9) + 2 (1 - (2 / 3)^(2 / 3))) +
       ((4 * Pi^2 * nu) / Abs[L]) * Abs[k]^((2 / 3) - (4 / 9) + 2 (1 - (2 / 3)^(2 / 3)) + (4 / 3))) +
    (((Sqrt[2 / Pi] * Abs[a] / (a^2 + k^m)))^2 /
      ((Abs[k])^((2 / 3) - (4 / 9) + 2 (1 - (2 / 3)^(2 / 3))) + ((8 * Pi^2 * nu) / Abs[L]) *
         (Abs[k]^((2 / 3) - (4 / 9) + 2 (1 - (2 / 3)^(2 / 3)) + (4 / 3))) +
        ((16 * Pi^4 * nu^2) / L^2) * (Abs[k]^((2 / 3) - (4 / 9) + 2 (1 - (2 / 3)^(2 / 3))) +
            (8 / 3)))))) * (Abs[Sin[Pi * k * r / (19540.3 (R))]])^2
(*Second structure function formula*)

v2 =
  ReadList["C:\\Users\\John\\Desktop\\MPIDSReLambda110\\110SecondStructureFunction.txt",
   "Number"];
(*Data for second structure function*)

x = ReadList["C:\\Users\\John\\Desktop\\MPIDSRELambda264\\RoverEta.txt", "Number"];

y2 = v2 / (x^((2 / 3) - (4 / 9) + 2 (1 - (2 / 3)^(2 / 3))));
(*Compensating the second structure function by r^(zeta_2)*)

u2 = Transpose[{x, y2}];

q2 = Transpose[{x, v2}];
```

```
FindFit[u2, (A1 * Abs[Sin[Pi * r / (19540.3 (1.56917))]]^2 +
     A2 * Abs[Sin[Pi * r * 2 / (19540.3 (1.56917))]]^2 +
     Sum[g[k, r, L, .00001546, 11.6425, 0.0161237, m, 1.56917], {k, 3, 1000}]) /
   (r^((2/3) - (4/9) + 2 (1 - (2/3)^(2/3)))),
 {L, {m, 1.3}, A1, A2}, r, MaxIterations → 10000]
(*Fitting the second structure function*)
```

```
{L → 2.79532, m → 1.56268, A1 → 0.00743913, A2 → 0.00285281}
```

```
Show[LogLogPlot[(0.00743913 * Abs[Sin[Pi * r / (19540.3 (1.56917))]]^2 +
     0.00285281 * Abs[Sin[Pi * r * 2 / (19540.3 (1.56917))]]^2 +
     Sum[g[k, r, 2.79532, .00001546, 11.6425, 0.0161237, 1.56268, 1.56917], {k, 3, 1000}]),
   {r, 1.95403, Max[q2]}, PlotRange → All, PlotStyle → {Red, Thick}, TicksStyle → Larger],
 ListLogLogPlot[q2, PlotRange → All, PlotMarkers → {◇, 20}]]
(*Plot of the results of the second structure
  function fit against the data on a log-log scale*)
```

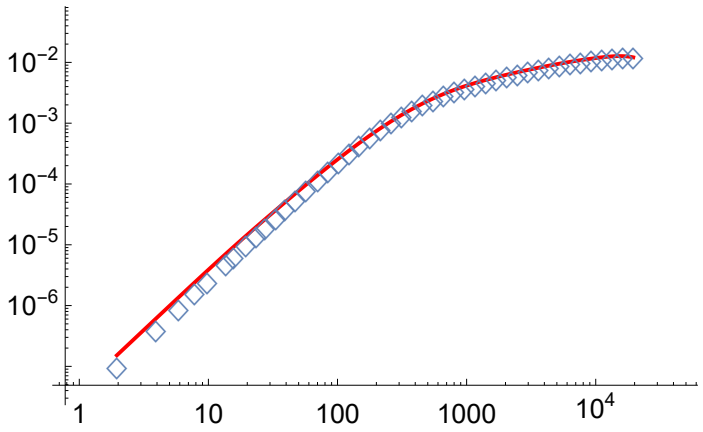


```
Show[Plot[(0.00743913 * Abs[Sin[Pi * r / (19540.3 (1.56917))]]^2 +
     0.00285281 * Abs[Sin[Pi * r * 2 / (19540.3 (1.56917))]]^2 +
     Sum[g[k, r, 2.79532, .00001546, 11.6425, 0.0161237, 1.56268, 1.56917], {k, 3, 1000}]),
   {r, 1.95403, Max[q2]}, PlotRange → All, PlotStyle → {Red, Thick}, TicksStyle → Larger],
 ListPlot[q2, PlotRange → All, PlotMarkers → {◇, 20}]]
(*Plot of the results of the second structure function
 fit against the data on a normal scale*)
```

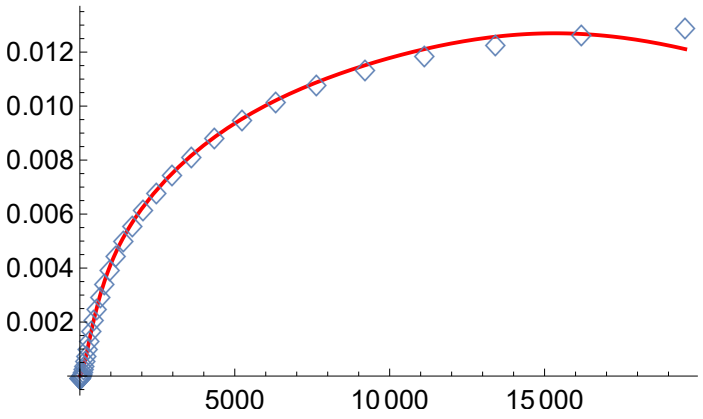

```
f[k_, r_, L_, nu_, a_, b_, m_, R_] :=
 (16 / L^4) * (((L^2 / 4) * ((Sqrt[2 / Pi] * Abs[b] / (b^2 + k^m)))^2) /
     (Abs[k]^((4 / 3) - (8 / 9) + 2 (1 - (2 / 3)^(4 / 3))) +
       (8 * Pi^2 * nu / L) * Abs[k]^((4 / 3) - (8 / 9) + 2 (1 - (2 / 3)^(4 / 3)) + (4 / 3)) +
       (16 * Pi^4 * nu^2 / L^2) * Abs[k]^((4 / 3) - (8 / 9) + 2 (1 - (2 / 3)^(4 / 3)) + 8 / 3)) +
    ((L / 2) * ((Sqrt[2 / Pi] * Abs[b] / (b^2 + k^m))) * Abs[Sqrt[2 / Pi] * Abs[a] / (a^2 + k^m)]^
        2) / (Abs[k]^((4 / 3) - (8 / 9) + 2 (1 - (2 / 3)^(4 / 3))) +
       (12 * Pi^2 * nu / L) * Abs[k]^((4 / 3) - (8 / 9) + 2 (1 - (2 / 3)^(4 / 3)) + (4 / 3)) +
       (48 * Pi^4 * nu^2 / L^2) * Abs[k]^((4 / 3) - (8 / 9) + 2 (1 - (2 / 3)^(4 / 3)) + (8 / 3)) +
       (64 * Pi^6 * nu^3 / L^3) * Abs[k]^((4 / 3) - (8 / 9) + 2 (1 - (2 / 3)^(4 / 3)) + 4)) +
    (Abs[Sqrt[2 / Pi] * Abs[a] / (a^2 + k^m)])^4 /
     (Abs[k]^((4 / 3) - (8 / 9) + 2 (1 - (2 / 3)^(4 / 3))) +
       (16 * Pi^2 * nu / L) * Abs[k]^((4 / 3) - (8 / 9) + 2 (1 - (2 / 3)^(4 / 3)) + (4 / 3)) +
       (96 * Pi^4 * nu^2 / L^2) * Abs[k]^((4 / 3) - (8 / 9) + 2 (1 - (2 / 3)^(4 / 3)) + (8 / 3)) +
       (256 * Pi^6 * nu^3 / L^3) * Abs[k]^((4 / 3) - (8 / 9) + 2 (1 - (2 / 3)^(4 / 3)) + 4) +
       (256 * Pi^8 * nu^4 / L^4) * Abs[k]^((4 / 3) - (8 / 9) + 2 (1 - (2 / 3)^(4 / 3)) +
           (16 / 3)))) * Abs[Sin[Pi * k * r / (19540.3 (R))]]^4
(*Fourth structure function formula*)

v4 =
  ReadList["C:\\Users\\John\\Desktop\\MPIDSReLambda110\\110FourthStructureFunction.txt",
   "Number"];
(*Fourth structure function data*)

y4 = v4 / (x^((4 / 3) - (8 / 9) + 2 (1 - (2 / 3)^(4 / 3))));
(*Compensating the fourth structure function*)

u4 = Transpose[{x, y4}];

q4 = Transpose[{x, v4}];

FindFit[u4,
 (A1 * Abs[Sin[Pi * r / (19540.3 (R))]]^4 + A2 * Abs[Sin[Pi * r * 2 / (19540.3 (R))]]^4 +
    Sum[f[k, r, L, .00001546, a, b, m, R], {k, 3, 1000}]) /
  (r^((4 / 3) - (8 / 9) + 2 (1 - (2 / 3)^(4 / 3)))), {{L, .5}, {a, 10}, b,
  {m, 1.3}, {R, 1.5}, A1, A2}, r, MaxIterations → 10000]
(*Fitting the fourth structure function.  Note that this is where a,
b, and R are set for the entire Taylor Reynolds number*)

{L → 1.0749, a → 11.6425, b → 0.0161237,
 m → 1.26897, R → 1.56917, A1 → 0.000383851, A2 → 0.000174405}
```

```
Show[LogLogPlot[(0.000383851 * Abs[Sin[Pi * r / (19540.3 (1.56917))]]^4 +
     0.000174405 * Abs[Sin[Pi * r * 2 / (19540.3 (1.56917))]]^4 +
     Sum[f[k, r, 1.0749, .00001546, 11.6425, 0.0161237, 1.26897, 1.56917], {k, 3, 1000}]),
  {r, 1.95403, Max[q4]}, PlotRange → All, PlotStyle → {Red, Thick}, TicksStyle → Larger],
 ListLogLogPlot[q4, PlotRange → All, PlotMarkers → {◇, 20}]]
(*Plot of the results of the fourth structure
  function fit against the data on a log-log scale*)
```

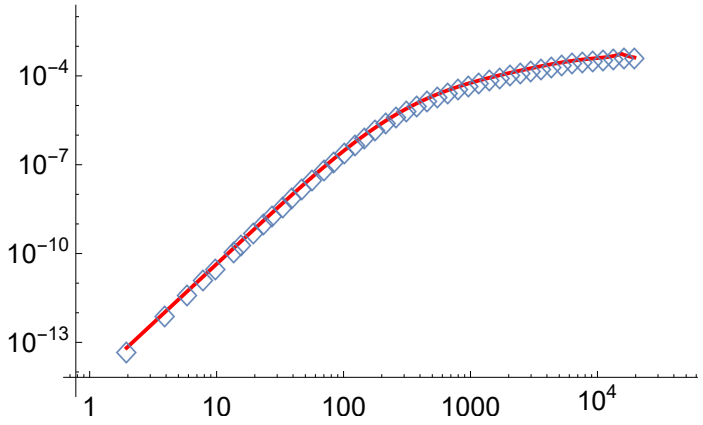

```
p[k_, r_, L_, nu_, a_, b_, m_, R_] := (2 / L) ^6 * ((8 / L^3) *
     (((Sqrt[2 / Pi] * Abs[b] / (b^2 + k^m)) ^3) / (Abs[k] ^ (2 - (12 / 9) + 2 (1 - (2 / 3) ^2)) +
          (12 * Pi^2 * nu / L) * Abs[k] ^ ((2 - (12 / 9) + 2 (1 - (2 / 3) ^2)) + (4 / 3)) +
          (48 * Pi^4 * nu^2 / L^2) * Abs[k] ^ ((2 - (12 / 9) + 2 (1 - (2 / 3) ^2)) + (8 / 3)) +
          (64 * Pi^6 * nu^3 / L^3) * Abs[k] ^ ((2 - (12 / 9) + 2 (1 - (2 / 3) ^2)) + 4)) +
       ((4 / L^2) * ((Sqrt[2 / Pi] * Abs[b] / (b^2 + k^m)) ^2) *
         ((Sqrt[2 / Pi] * Abs[a] / (a^2 + k^m)) ^2) / (Abs[k] ^ (2 - (12 / 9) + 2 (1 - (2 / 3) ^2)) +
            (16 * Pi^2 * nu / L) * Abs[k] ^ ((2 - (12 / 9) + 2 (1 - (2 / 3) ^2)) + (4 / 3)) +
            (96 * Pi^4 * nu^2 / L^2) * Abs[k] ^ ((2 - (12 / 9) + 2 (1 - (2 / 3) ^2)) + (8 / 3)) +
            (256 * Pi^6 * nu^3 / L^3) * Abs[k] ^ ((2 - (12 / 9) + 2 (1 - (2 / 3) ^2)) + 4) +
            (256 * Pi^8 * nu^4 / L^4) * Abs[k] ^ ((2 - (12 / 9) + 2 (1 - (2 / 3) ^2)) + (16 / 3)))) +
       ((2 / L) * (Sqrt[2 / Pi] * Abs[b] / (b^2 + k^m)) *
         ((Sqrt[2 / Pi] * Abs[a] / (a^2 + k^m)) ^4) / (Abs[k] ^ (2 - (12 / 9) + 2 (1 - (2 / 3) ^2)) +
            (20 * Pi^2 * nu / L) * Abs[k] ^ ((2 - (12 / 9) + 2 (1 - (2 / 3) ^2)) + (4 / 3)) +
            (160 * Pi^4 * nu^2 / L^2) * Abs[k] ^ ((2 - (12 / 9) + 2 (1 - (2 / 3) ^2)) + (8 / 3)) +
            (640 * Pi^6 * nu^3 / L^3) * Abs[k] ^ ((2 - (12 / 9) + 2 (1 - (2 / 3) ^2)) + 4) +
            (1280 * Pi^8 * nu^4 / L^4) * Abs[k] ^ ((2 - (12 / 9) + 2 (1 - (2 / 3) ^2)) + (16 / 3)) +
            (1024 * Pi^10 * nu^5 / L^5) *
             Abs[k] ^ ((2 - (12 / 9) + 2 (1 - (2 / 3) ^2)) + (20 / 3)))) +
       ((Sqrt[2 / Pi] * Abs[a] / (a^2 + k^m)) ^6 / (Abs[k] ^ (2 - (12 / 9) + 2 (1 - (2 / 3) ^2)) +
          (24 * Pi^2 * nu / L) * Abs[k] ^ ((2 - (12 / 9) + 2 (1 - (2 / 3) ^2)) + (4 / 3)) +
          (240 * Pi^4 * nu^2 / L^2) * Abs[k] ^ ((2 - (12 / 9) + 2 (1 - (2 / 3) ^2)) + (8 / 3)) +
          (1280 * Pi^6 * nu^3 / L^3) * Abs[k] ^ ((2 - (12 / 9) + 2 (1 - (2 / 3) ^2)) + 4) +
          (3480 * Pi^8 * nu^4 / L^4) * Abs[k] ^ ((2 - (12 / 9) + 2 (1 - (2 / 3) ^2)) + (16 / 3)) +
          (6144 * Pi^10 * nu^5 / L^5) * Abs[k] ^ ((2 - (12 / 9) + 2 (1 - (2 / 3) ^2)) + (20 / 3)) +
          (4096 * Pi^12 * nu^6 / L^6) * Abs[k] ^ ((2 - (12 / 9) + 2 (1 - (2 / 3) ^2)) + 8))))) *
  Abs[Sin[Pi * k * r / (19540.3 (R))]] ^
   6
(*Sixth structure function formula*)

v6 = ReadList["C:\\Users\\John\\Desktop\\MPIDSReLambda110\\110SixthStructureFunction.txt",
   "Number"];
(*Sixth structure function data*)

x = ReadList["C:\\Users\\John\\Desktop\\MPIDSRELambda264\\RoverEta.txt", "Number"];

y6 = v6 / (x^ ((6 / 3) - (12 / 9) + 2 (1 - (2 / 3) ^ (6 / 3))));
(*Compensating the sixth structure function*)

u6 = Transpose[{x, y6}];

q6 = Transpose[{x, v6}];
```

```
FindFit[u6, (A1 * Abs[Sin[Pi * r / (19540.3 (1.56917))]]^6 +
     A2 * Abs[Sin[Pi * r * 2 / (19540.3 (1.56917))]]^6 +
     Sum[p[k, r, L, .00001546, 11.6425, 0.0161237, m, 1.56917], {k, 3, 1000}]) /
   (r^((6/3) - (12/9) + 2 (1 - (2/3)^(6/3)))),
 {L, {m, 1.3}, A1, A2}, r, MaxIterations → 10000]
(*Fitting the sixth structure function*)
```

$$\{L \to 1.15286,\ m \to 0.986067,\ A1 \to 0.0000341082,\ A2 \to 4.23641 \times 10^{-6}\}$$

```
Show[LogLogPlot[(0.0000341082 * Abs[Sin[Pi * r / (19540.3 (1.56917))]]^6 +
     4.23641 * (10^(-6)) * Abs[Sin[Pi * r * 2 / (19540.3 (1.56917))]]^6 +
     Sum[p[k, r, 1.15286, .00001546, 11.6425, 0.0161237, .986067, 1.56917], {k, 3, 1000}]),
   {r, 1.95403, Max[q6]}, PlotRange → All, PlotStyle → {Red, Thick}, TicksStyle → Larger],
 ListLogLogPlot[q6, PlotRange → All, PlotMarkers → {◇, 20}]]
(*Plot of the results of the sixth structure
  function fit against the data on a log-log scale*)
```

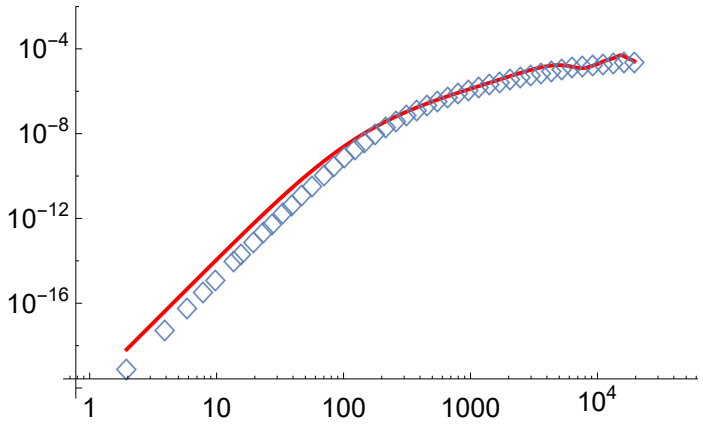


```
q[k_, r_, L_, nu_, a_, b_, m_, R_] :=
 (2/L)^8 * ((((L^4/16) * (Sqrt[2/Pi] * Abs[b] / (b^2 + k^m))^4 /
         (Abs[k]^((8/3) - (16/9) + 2 (1 - (2/3)^(8/3))) +
           (16 * Pi^2 * nu / L) * Abs[k]^((8/3) - (16/9) + 2 (1 - (2/3)^(8/3)) + (4/3)) +
           (96 * Pi^4 * nu^2 / L^2) * Abs[k]^
             ((8/3) - (16/9) + 2 (1 - (2/3)^(8/3)) + (8/3)) + (256 * Pi^6 * nu^3 / L^3) *
            Abs[k]^((8/3) - (16/9) + 2 (1 - (2/3)^(8/3)) + 4) + (256 * Pi^8 * nu^4 / L^4) *
            Abs[k]^((8/3) - (16/9) + 2 (1 - (2/3)^(8/3)) + (16/3)))) +
     ((L^3/8) * (Sqrt[2/Pi] * Abs[b] / (b^2 + k^m))^3 *
       (Sqrt[2/Pi] * Abs[a] / (a^2 + k^m))^2 /
        (Abs[k]^((8/3) - (16/9) + 2 (1 - (2/3)^(8/3))) + (20 * Pi^2 * nu / L) * Abs[k]^
             ((8/3) - (16/9) + 2 (1 - (2/3)^(8/3)) + (4/3)) + (160 * Pi^4 * nu^2 / L^2) *
            Abs[k]^((8/3) - (16/9) + 2 (1 - (2/3)^(8/3)) + (8/3)) +
           (640 * Pi^6 * nu^3 / L^3) * Abs[k]^((8/3) - (16/9) + 2 (1 - (2/3)^(8/3)) + 4) +
           (1280 * Pi^8 * nu^4 / L^4) * Abs[k]^
             ((8/3) - (16/9) + 2 (1 - (2/3)^(8/3)) + (16/3)) + (1024 * Pi^10 * nu^5 / L^5) *
            Abs[k]^((8/3) - (16/9) + 2 (1 - (2/3)^(8/3)) + (20/3)))) +
     ((L^2/4) * (Sqrt[2/Pi] * Abs[b] / (b^2 + k^m))^2 *
       (Sqrt[2/Pi] * Abs[a] / (a^2 + k^m))^4 /
```

```
          (Abs[k]^((8/3) - (16/9) + 2 (1 - (2/3)^(8/3))) + (24 * Pi^2 * nu / L) * Abs[k]^
                ((8/3) - (16/9) + 2 (1 - (2/3)^(8/3)) + (4/3)) + (240 * Pi^4 * nu^2 / L^2) *
              Abs[k]^((8/3) - (16/9) + 2 (1 - (2/3)^(8/3)) + (8/3)) +
             (1280 * Pi^6 * nu^3 / L^3) * Abs[k]^((8/3) - (16/9) + 2 (1 - (2/3)^(8/3)) + 4) +
             (3840 * Pi^8 * nu^4 / L^4) * Abs[k]^
               ((8/3) - (16/9) + 2 (1 - (2/3)^(8/3)) + (16/3)) + (6144 * Pi^10 * nu^5 / L^5) *
              Abs[k]^((8/3) - (16/9) + 2 (1 - (2/3)^(8/3)) + (20/3)) + (4096 * Pi^12 *
                nu^6 / L^6) * Abs[k]^((8/3) - (16/9) + 2 (1 - (2/3)^(8/3)) + 8))) +
       ((L/2) * (Sqrt[2/Pi] * Abs[b] / (b^2 + k^m)) * (Sqrt[2/Pi] * Abs[a] / (a^2 + k^m))^6 /
          (Abs[k]^((8/3) - (16/9) + 2 (1 - (2/3)^(8/3))) +
            (28 * Pi^2 * nu / L) * Abs[k]^((8/3) - (16/9) + 2 (1 - (2/3)^(8/3)) + (4/3)) +
            (336 * Pi^4 * nu^2 / L^2) * Abs[k]^
              ((8/3) - (16/9) + 2 (1 - (2/3)^(8/3)) + (8/3)) + (2240 * Pi^6 * nu^3 / L^3) *
             Abs[k]^((8/3) - (16/9) + 2 (1 - (2/3)^(8/3)) + 4) + (8960 * Pi^8 * nu^4 / L^4) *
             Abs[k]^((8/3) - (16/9) + 2 (1 - (2/3)^(8/3)) + (16/3)) +
            (21504 * Pi^10 * nu^5 / L^5) * Abs[k]^((8/3) - (16/9) +
                2 (1 - (2/3)^(8/3)) + (20/3)) + (28672 * Pi^12 * nu^6 / L^6) * Abs[k]^
              ((8/3) - (16/9) + 2 (1 - (2/3)^(8/3)) + 8) + (16384 * Pi^14 * nu^7 / L^7) *
             Abs[k]^((8/3) - (16/9) + 2 (1 - (2/3)^(8/3)) + (28/3)))) +
       (Sqrt[2/Pi] * Abs[a] / (a^2 + k^m))^8 /
        (Abs[k]^((8/3) - (16/9) + 2 (1 - (2/3)^(8/3))) +
          (32 * Pi^2 * nu / L) * Abs[k]^((8/3) - (16/9) + 2 (1 - (2/3)^(8/3)) + (4/3)) +
          (448 * Pi^4 * nu^2 / L^2) * Abs[k]^((8/3) - (16/9) + 2 (1 - (2/3)^(8/3)) + (8/3)) +
          (3584 * Pi^6 * nu^3 / L^3) * Abs[k]^((8/3) - (16/9) + 2 (1 - (2/3)^(8/3)) + 4) +
          (17920 * Pi^8 * nu^4 / L^4) * Abs[k]^
            ((8/3) - (16/9) + 2 (1 - (2/3)^(8/3)) + (16/3)) + (57344 * Pi^10 * nu^5 / L^5) *
           Abs[k]^((8/3) - (16/9) + 2 (1 - (2/3)^(8/3)) + (20/3)) +
          (114688 * Pi^12 * nu^6 / L^6) * Abs[k]^((8/3) - (16/9) + 2 (1 - (2/3)^(8/3)) + 8) +
          (131072 * Pi^14 * nu^7 / L^7) * Abs[k]^
            ((8/3) - (16/9) + 2 (1 - (2/3)^(8/3)) + (28/3)) + (65536 * Pi^16 * nu^8 / L^8) *
           Abs[k]^((8/3) - (16/9) + 2 (1 - (2/3)^(8/3)) + (32/3))))) *
  Abs[Sin[Pi * k * r / (19540.3 (R))]]^
   8
(*Eighth structure function formula*)

v8 =
  ReadList["C:\\Users\\John\\Desktop\\MPIDSReLambda110\\110EighthStructureFunction.txt",
   "Number"];
(*Eighth structure function data*)

x = ReadList["C:\\Users\\John\\Desktop\\MPIDSRELambda264\\RoverEta.txt", "Number"];

y8 = v8 / (x^((8/3) - (16/9) + 2 (1 - (2/3)^(8/3))));
(*Compensating the eighth structure function*)

u8 = Transpose[{x, y8}];

p8 = Transpose[{x, v8}];
```

```
FindFit[u8, (A1 * Abs[Sin[Pi * r / (19540.3 (1.56917))]]^8 +
     A2 * Abs[Sin[Pi * r * 2 / (19540.3 (1.56917))]]^8 +
     Sum[q[k, r, L, .00001546, 11.6425, 0.0161237, m, 1.56917], {k, 3, 1000}]) /
   (r^((8/3) - (16/9) + 2 (1 - (2/3)^(8/3)))),
 {{L, 0.1}, {m, 0.75}, A1, A2}, r, MaxIterations → 10000]
(*Fitting the eighth structure function*)
```

$$\{L \to 0.615824,\ m \to 0.971146,\ A1 \to 3.11806 \times 10^{-6},\ A2 \to 1.03704 \times 10^{-6}\}$$

```
Show[LogLogPlot[(3.11806 * 10^(-6) * Abs[Sin[Pi * r / (19540.3 (1.56917))]]^8 +
     1.03704 * 10^(-6) * Abs[Sin[Pi * r * 2 / (19540.3 (1.56917))]]^8 +
     Sum[q[k, r, .615824, .00001546, 11.6425, 0.0161237, .971146, 1.56917], {k, 3, 1000}]),
  {r, 1.95403, Max[p8]}, PlotRange → All, PlotStyle → {Red, Thick}, TicksStyle → Larger],
 ListLogLogPlot[p8, PlotRange → All, PlotMarkers → {◇, 20}]]
(*Plot of the results of the eighth structure
  function fit against the data on a log-log scale*)
```

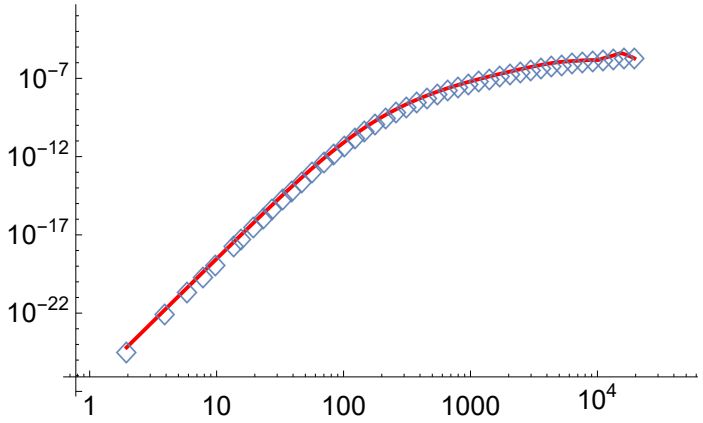

Bibliography

[1] B. Birnir, *The Kolmogorov-Obukhov statistical theory of turbulence*, *J. Nonlinear Sci.* (2013). DOI 10.1007/s00332-012-9164-z.

[2] E. Bodenschatz, G. P. Bewley, H. Nobach, M. Sinhuber, and H. Xu, *Variable density turbulence tunnel facility*, *Review of Scientific Instruments* **85** (2014), no. 9 093908.

[3] L. D. Landau and E. M. Lifshits, *Fluid Mechanics: Transl. from the Russian by JB Sykes and WH Reid*. Addison-Wesley, 1959.

[4] Z.-S. She and E. Leveque, *Universal scaling laws in fully developed turbulence*, *Phys. Rev. Letters* **72** (1994), no. 3 336–339.

[5] B. Dubrulle, *Intermittency in fully developed turbulence: in log-Poisson statistics and generalized scale covariance*, *Phys. Rev. Letters* **73** (1994), no. 7 959–962.

[6] Z.-S. She and E. Waymire, *Quantized energy cascade and log-poisson statistics in fully developed turbulence*, *Phys. Rev. Letters* **74** (1995), no. 2 262–265.

[7] S. B. Pope, *Turbulent Flows*. Cambridge Univ. Press, Cambridge UK, 2000.

[8] J. B. Walsh, *An Introduction to Stochastic Differential Equations*. Springer Lecture Notes, eds. A. Dold and B. Eckmann, Springer, New York, 1984.

[9] B. Birnir, *The Kolmogorov-Obukhov Theory of Turbulence*. Springer, New York, 2013.

[10] B. Birnir, X. Chen, and Z.-S. She, *Moments and probability density functions in turbulent boundary layers*, *CNLS preprint to appear* (2015).

[11] B. Birnir, *From Wind-Blown Sand to Turbulence and Back*, pp. 15–27. Springer International Publishing, Cham, 2016.

[12] O. E. Barndorff-Nilsen, *Exponentially decreasing distributions for the logarithm of the particle size*, *Proc. R. Soc. London* **A 353** (1977) 401–419.

[13] O. Reynolds, *On the dynamical theory of incompressible viscous fluids and the determination of the criterion.*, *Phil. Trans. Roy. Soc. Lond.* **186A** (1885) 123–164.

[14] P. S. Bernard and J. M. Wallace, *Turbulent Flow*. John Wiley & Sons, Hoboken, NJ, 2002.

[15] A. N. Kolmogorov, *The local structure of turbulence in incompressible viscous fluid for very large Reynolds number*, *Dokl. Akad. Nauk SSSR* **30** (1941) 9–13.

[16] A. N. Kolmogorov, *Dissipation of energy under locally istotropic turbulence*, *Dokl. Akad. Nauk SSSR* **32** (1941) 16–18.

[17] A. N. Kolmogorov, *A refinement of previous hypotheses concerning the local structure of turbulence in a viscous incompressible fluid at high Reynolds number*, *J. Fluid Mech.* **13** (1962) 82–85.

[18] G. Grimmett and D. Stirzaker, *Probability and Random Processes*. 3 ed.

[19] R. Bhattacharya and E. C. Waymire, *Stochastic Processes with Application*. John Wiley, New York, 1990.

[20] B. Oksendal, *Stochastic Differential Equations*. Springer, New York, 1998.

[21] G. Da Prato and J. Zabczyk, *Encyclopedia of Mathematics and its Applications: Stochastic Equations in Infinite Dimensions*. Cambridge University Press, 2014.

[22] D. D. Baals and W. R. Corliss, *Wind tunnels of NASA*, vol. 440. Scientific and Technical Information Branch, National Aeronautics and Space Administration, 1981.

[23] L. Prandtl, *Göttingen wind tunnel for testing aircraft models*, 1920.

[24] J. D. Anderson Jr, *A history of aerodynamics: and its impact on flying machines*, vol. 8. Cambridge University Press, 1999.

[25] G. I. Taylor, *Statistical theory of turbulence*, *Proc. Royal Soc. London* **151** (1935) 421–444.

[26] S. Corrsin, *Turbulent flow*, *American Scientist* **49** (1961), no. 3 300–325.

[27] G. Comte-Bellot and S. Corrsin, *The use of a contraction to improve the isotropy of grid-generated turbulence*, *Journal of Fluid Mechanics* **25** (1966), no. 04 657–682.

[28] C. Millikan, J. Smith, and R. Bell, *High-speed testing in the southern california cooperative wind tunnel*, *Journal of the Aeronautical Sciences* **15** (1948), no. 2 69–88.

[29] B. Hunt, T. Sauer, and J. Yorke, *Prevalence: A translation-invariant "almost every" on ininite-dimensional spaces*, *Bull. of the Am. Math. Soc.* **27** (1992), no. 2 217–238.

[30] M. Sinhuber, E. Bodenschatz, and G. P. Bewley, *Decay of turbulence at high reynolds numbers*, *Physical Review Letters* **114** (2015) 034501.

[31] L. Onsager, *The distribution of energy in turbulence*, *Phys. Rev.* **68** (1945) 285.

[32] L. Onsager, *Statistical hydrodynamics*, *Nuovo Cimento.* **6** (1945), no. 2 279–287.

[33] A. A. Townsend, *The Structure of Turbulent Shear Flow*. Cambridge University Press, 1976.

[34] A. E. Perry and M. S. Chong, *On the mechanism of wall turbulence.*, *J. Fluid Mech.* **119** (1982) 173–217.

[35] A. E. Perry and *et al. Journal of Fluid Mechanics* **165** (1986).

[36] I. Marusic and C. Meneveau, *Generalized logarithmic law for high-order moments in turbulent boundary layers*, *J. Fluid Mech.* **719, R1** (2013) 1–11.

[37] C. M. de Silva and *et al. Journal of Fluid Mechanics* **769** (2015).

[38] R. J. A. M. Stevens and *et al. Journal of Fluid Mechanics* **757** (2014).

[39] P. Vincenti, J. Klewicki, C. Morrill-Winter, C. M. White, and M. Wosnik, *Streamwise velocity statistics in turbulent boundary layers that spatially develop to high reynolds number*, *Experimental Fluids* (2013).